



Global Biogeochemical Cycles^a



RESEARCH ARTICLE

10.1029/2023GB007837

Key Points:

- Iron in phytoplankton accounts for <80% of chemically labile Fe and does not exceed 0.1 nM
- Biogenic Fe is a small and relatively invariant component of particulate Fe (PFe) pools, even across seasonal and regional gradients
- Authigenic Fe is a significant fraction of particulate Fe across seasons and productivity gradients

Supporting Information:

Supporting Information may be found in the online version of this article.

Correspondence to:

B. S. Twining, btwining@bigelow.org

Citation:

Sofen, L. E., Antipova, O. A., Buck, K. N., Caprara, S., Chacho, L., Johnson, R. J., et al. (2023). Authigenic iron is a significant component of oceanic labile particulate iron inventories. *Global Biogeochemical Cycles*, 37, e2023GB007837. https://doi.org/10.1029/2023GB007837

Received 9 MAY 2023 Accepted 23 OCT 2023

Author Contributions:

Conceptualization: Kristen N. Buck, Rodney J. Johnson, Daniel C. Ohnemus, Peter N. Sedwick, Alessandro Tagliabue, Benjamin S. Twining

Data curation: Laura E. Sofen **Formal analysis:** Laura E. Sofen, Sara Rauschenberg

Funding acquisition: Kristen N. Buck, Rodney J. Johnson, Daniel C. Ohnemus, Peter N. Sedwick, Alessandro Tagliabue, Benjamin S. Twining

© 2023. The Authors.

This is an open access article under the terms of the Creative Commons Attribution License, which permits use, distribution and reproduction in any medium, provided the original work is properly cited.

Authigenic Iron Is a Significant Component of Oceanic Labile Particulate Iron Inventories

Laura E. Sofen¹, Olga A. Antipova², Kristen N. Buck^{3,4}, Salvatore Caprara³, Lauren Chacho^{1,5}, Rodney J. Johnson⁶, Gabriella Kim^{1,7}, Peter Morton^{8,9,10}, Daniel C. Ohnemus¹¹, Sara Rauschenberg¹, Peter N. Sedwick¹², Alessandro Tagliabue¹³, and Benjamin S. Twining¹

¹Bigelow Laboratory for Ocean Sciences, East Boothbay, ME, USA, ²X-Ray Science Division, Advanced Photon Source, Argonne National Laboratory, Lemont, IL, USA, ³College of Marine Science, University of South Florida, St. Petersburg, FL, USA, ⁴Now at College of Earth, Ocean, and Atmospheric Sciences, Oregon State University, Corvallis, OR, USA, ⁵Northeastern University, Boston, MA, USA, ⁶Bermuda Institute of Ocean Sciences, St. Georges, Bermuda, ⁷Colby College, Waterville, ME, USA, ⁸National High Magnetic Field Lab, Geochemistry Group, Tallahassee, FL, USA, ⁹Department of Earth, Ocean and Atmospheric Science, Florida State University, Tallahassee, FL, USA, ¹⁰Now at Department of Oceanography, Texas A&M University, College Station, Texas, USA, ¹¹Skidaway Institute of Oceanography, University of Georgia, Savannah, GA, USA, ¹²Department of Ocean and Earth Sciences, Old Dominion University, Norfolk, VA, USA, ¹³School of Environmental Sciences, University of Liverpool, Liverpool, UK

Abstract Particulate phases transport trace metals (TM) and thereby exert a major control on TM distribution in the ocean. Particulate TMs can be classified by their origin as lithogenic (crustal material), biogenic (cellular), or authigenic (formed in situ), but distinguishing these fractions analytically in field samples is a challenge often addressed using operational definitions and assumptions. These different phases require accurate characterization because they have distinct roles in the biogeochemical iron cycle. Particles collected from the upper 2,000 m of the northwest subtropical Atlantic Ocean over four seasonal cruises throughout 2019 were digested with a chemical leach to operationally distinguish labile particulate material from refractory lithogenics. Direct measurements of cellular iron (Fe) were used to calculate the biogenic contribution to the labile Fe fraction, and any remaining labile material was defined as authigenic. Total particulate Fe (PFe) inventories varied <15% between seasons despite strong seasonality in dust inputs. Across seasons, the total PFe inventory (\pm 1SD) was composed of 73 \pm 13% lithogenic, 18 \pm 7% authigenic, and 10 \pm 8% biogenic Fe above the deep chlorophyll maximum (DCM), and 69 \pm 8% lithogenic, 30 \pm 8% authigenic, and 1.1 \pm 0.5% biogenic Fe below the DCM. Data from three other ocean regions further reveal the importance of the authigenic fraction across broad productivity and Fe gradients, comprising ca. 20%–27% of total PFe.

Plain Language Summary The availability of dissolved iron controls phytoplankton growth in much of the ocean. Most oceanic iron is contained in particles that are a mixture of live and dead cells (biogenics), crustal material (lithogenics), and minerals that have precipitated in seawater (authigenics). Each of these materials has different chemical properties that determine how iron cycles through the ocean and regulate how much iron is available for uptake by phytoplankton. Specifically, authigenic and biogenic forms are more accessible to phytoplankton but are often measured as one fraction despite formation by different processes. We measured different forms of iron in particles across seasons and environmental gradients and found that 20%–30% of iron is authigenic.

1. Introduction

Particulate forms of trace metals (TMs) play an important role in controlling dissolved TM concentrations in the ocean (Boyd & Ellwood, 2010; Milne et al., 2017; Ohnemus et al., 2019) and as a direct source of TM micronutrients to marine phytoplankton communities (Hurst et al., 2010; van der Merwe et al., 2019). Marine particle assemblages are heterogeneous and include crustal minerals (lithogenic), cellular material (biogenic), and phases precipitated in situ (authigenic) (Table 1). The different sources and chemical forms of these fractions are reflected by distinct dynamics in the water column, with significant implications for oceanic TM cycling. Dissolved iron (DFe) distributions in the interior are strongly controlled by internal cycling processes as much as by physical transport to the ocean interior (Tagliabue et al., 2019). Biogeochemical models that represent the details of internal cycling capture observed iron (Fe) distributions better than simpler representations of the

SOFEN ET AL. 1 of 23



Global Biogeochemical Cycles

10.1029/2023GB007837

Antipova, Lauren Chacho, Rodney J. Johnson, Gabriella Kim, Peter Morton, Daniel C. Ohnemus, Sara Rauschenberg, Alessandro Tagliabue, Benjamin S. Twining Methodology: Alessandro Tagliabue, Benjamin S. Twining Project Administration: Peter N. Sedwick, Benjamin S. Twining Resources: Benjamin S. Twining Supervision: Benjamin S. Twining Visualization: Laura E. Sofen Writing - original draft: Laura E. Sofen Writing - review & editing: Laura E. Sofen, Kristen N. Buck, Salvatore Caprara, Lauren Chacho, Rodney J.

Johnson, Daniel C. Ohnemus, Peter N. Sedwick, Alessandro Tagliabue,

Benjamin S. Twining

Investigation: Laura E. Sofen, Olga A.

Fe cycle, but so far, no model captures all observed spatial features of Fe in the ocean. Global-scale Fe models produce a large range of residence times for DFe (Tagliabue et al., 2016). Similarly, measurement-based estimates of particulate Fe (PFe) residence times in the surface ocean span up to five orders of magnitude (Black et al., 2020), highlighting the need for a better understanding of the processes that govern the ocean Fe cycle.

Geological, biological, and chemical processes determine particulate concentrations in the ocean water column. Lithogenic material arrives in the ocean via atmospheric deposition and sediment resuspension, and is chemically refractory. This fraction is predominantly silicate minerals, with titanium (Ti), aluminum (Al), and Fe stoichiometries that reflect source materials (Taylor & McLennan, 1995). The biogenic fraction is formed through cellular uptake, and remineralization of cellular detritus returns constituents to the dissolved fraction. Elemental stoichiometries of these particles reflect biological uptake and accumulation in living biomass (Twining & Baines, 2013) and differential remineralization from dead biomass (Twining et al., 2014). Authigenic fractions form via precipitation and scavenging of sparingly soluble or particle-reactive species, often forming as coatings of Fe and Mn oxides on other particles and may redissolve where chemically favorable (Jensen et al., 2020; Landing & Bruland, 1987). The combination of biologically driven uptake and remineralization along with abiotic authigenic phase formation and dissolution is referred to as internal cycling, and appears more important than external inputs to setting the distribution of DFe in the ocean interior (Tagliabue et al., 2019). The centrality of particle processes in controlling DFe thus highlights the need to measure and quantify particulate concentrations, in addition to dissolved concentrations, to draw conclusions about major Fe cycling processes. Given the complex partitioning of Fe across the three distinct particulate phases, it is important to understand the phase distributions in the water column.

Despite long-standing recognition of the existence of authigenic Fe (Goldberg, 1954), measurements are relatively sparse compared to those of lithogenic and biogenic fractions. Historically, many studies did not attempt to quantify authigenic Fe as a separate non-lithogenic phase (Table S1 in Supporting Information S1; Boyd et al., 2010; Buat-Menard & Chesselet, 1979; Gourain et al., 2019; Lemaitre et al., 2016; Marsay et al., 2018). Other studies have quantified mineral phases that are selective to specific chemical leaches, but these may include only a portion of the authigenic minerals (e.g., oxalate wash (Tovar-Sanchez et al., 2003) or 25% acetic acid (Hurst & Bruland, 2007)) and/or may include a portion of both authigenic and biogenic minerals (Berger et al., 2008). Recent approaches to quantifying the authigenic fraction calculate it from difference (Black et al., 2020; Lemaitre et al., 2020; Marsay et al., 2017). While lithogenic and biogenic particulate fractions can often be estimated using direct elemental proxies (e.g., Al or Ti and C or P, respectively), authigenic phases like Mn- and Fe-oxides and any associated sorbed TMs typically lack clear "end member" signatures and therefore cannot be easily directly estimated from bulk elemental analyses. Estimates of authigenic phases calculated by difference are subject to major uncertainties as a result of natural variability in the ratios of Al/Ti and TM/P used to estimate contributions of lithogenic and biogenic fractions, respectively. The end members can be poorly known and inputs of lithogenic and biogenic materials vary temporally. An alternative approach would use an operational definition of the lithogenic fraction and direct measurements of the biogenic fraction.

Here, we combine direct measurements of the biogenic fraction of PTMs with a well-characterized chemical leach for the labile phase to distinguish the various PFe fractions and examine their distribution, behavior, and importance over the course of a year in the upper water column of the western subtropical North Atlantic Ocean. We compare measurements using the chemical leach to those using Al as a tracer of lithogenic material. We then compare results from this region to other marine environments—near-shore and off-shore regions of the western Arctic, upwelling along the California coast, and high-nutrient, low-chlorophyll (HNLC) sub-Antarctic waters.

2. Materials and Methods

2.1. Cruise Summary

As part of the Bermuda Atlantic Iron Time-series (BAIT) project (GEOTRACES process study GApr13), four cruises were conducted in conjunction with regular sampling for the Bermuda Atlantic Time-series Study (BATS) during 2019 (Table S2 in Supporting Information S1): March 10–15 (BAIT-I, BATS cruise 357, RV *Endeavor*), May 11–17 (BAIT-II, BATS 359, RV *Atlantic Explorer*), August 16–22 (BAIT-III, BATS 362, RV *Atlantic Explorer*), and November 15–21 (BAIT IV, BATS 365, RV *Atlantic Explorer*). Each cruise sampled the BATS station (31.7°N, 64.2°W) and two adjacent spatial stations within 40–60 km of BATS that were nominally

SOFEN ET AL. 2 of 23

19449224, 2023, 1 2, Dowloaded from https://appubs.onlinelibary.wiley.com/doi/10.1029/2023GB007837, Wiley Online Library on [14/12/2023]. See the Terms and Conditions (https://onlinelibary.wiley.com/terms-and-conditions) on Wiley Online Library for rules of use; OA articles are governed by the applicable Creative Commons Licensia

Particulate iron fraction	Total PFe (PFe _{Total})					
	Lithogenic (PFe _{Lith})	Authigenic (PFe _{Auth}) (or "scavenged")	Biogenic (PFe _{Bio})			
		Labile PFe (PFe _{Labile})				
Operational iron fraction	Refractory (PFe _{Refrac})	Abiotic labile	Biotic labile			
Source	Terrestrial	Formed in situ	Biomass			
Chemical composition	Silicates, crystalline hydroxides and oxides	Oxyhydroxides	Cellular (metalloproteins, storage bodies, ions)			
Common proxies	Al, Ti	-	P, C			
	Strong acid	d digest (4M HCl/4M HNO ₃ /4M HF ^a)				
Chemical approaches		Oxalate rinse ^b ; HAc ^c or HAc/NH ₂ OH leach ^d				
This work: total—leach method						
Operational definition	Refractory	Abiotic labile	Biotic labile			
Calculation	$PFe_{Total} - PFe_{Labile}$	$PFe_{Labile} - PFe_{Bio}$	$PP \times POC:POP \times Fe:C$			
This work: proxy method						
Calculation	$PAl_{Total} \times Fe:Al$	_	_			

Note. PP, particulate phosphorus; Al, aluminum; Ti, titanium; POC, particulate organic carbon; POP, particulate organic phosphorus; Fe:C, cellular carbon-normalized iron quota of phytoplankton.

^aOhnemus et al. (2014). ^bTovar-Sanchez et al. (2003). ^cHurst and Bruland (2007). ^dBerger et al. (2008).

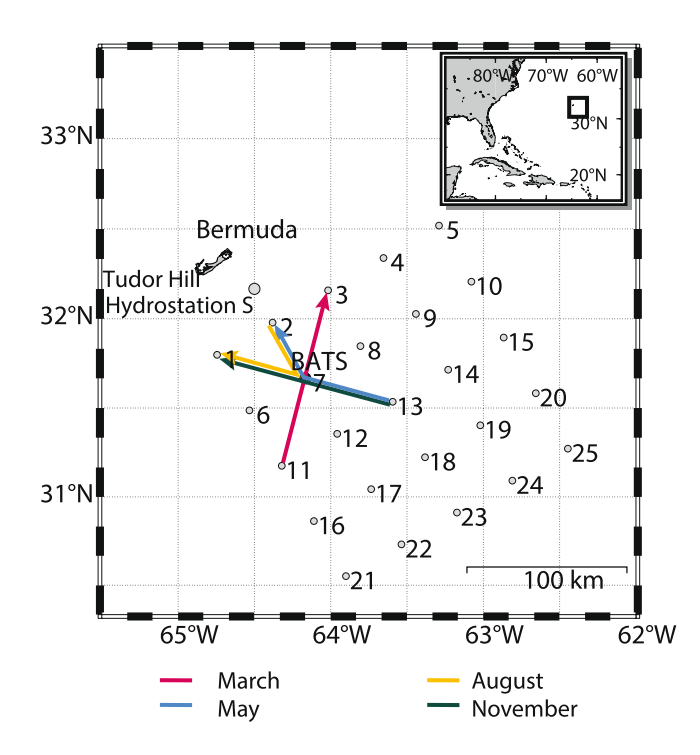


Figure 1. Bermuda Atlantic Iron Time-series project study region showing locations of Bermuda Atlantic Time-series Study and spatial stations where water column samples were collected and Tudor Hill on Bermuda where aerosols and rainwater were collected. Upstream-to-downstream paths for each sampling campaign are indicated by arrows. Map courtesy of Paul Lethaby.

selected to be "upstream" and "downstream" of BATS based on inferred regional circulation (Figure 1). The three stations for each cruise were treated as replicates of a single sampling location due to their proximity and strong overlap for the particulate elemental profiles.

2.2. Particle Sample Collection

Water column samples were collected between 20 and 1,700 m depth in 5 L Niskin-X bottles using a TM-clean CTD rosette (Sedwick et al., 2023) and filtered through 25 mm diameter 0.45 µm polyethersulfone membranes (Supor) for a maximum of 2 hr (2.35–4.05 L) to collect particles. Filters were pre-cleaned in 1 M HCl at 60°C overnight and washed with DI water to remove residual acid (Cutter et al., 2017). Filter samples were stored at -20°C until analysis. To provide a common reference between cruises, sampling depths always included the deep chlorophyll maximum (DCM), the dissolved oxygen minimum (OM), and density surfaces of σ = 26.1, 26.3, and 26.6 kg m $^{-3}$ (approx. 150, 350, and 500 m, respectively) based on data from immediately preceding BATS CTD casts. During the August cruise, TM CTD water-column samples were augmented by near-surface (2 m) samples collected in a hand-held Niskin-X sampler from a small boat that was positioned upwind and upstream of the research vessel to avoid contamination from the ship.

2.3. Elemental Concentrations of Particulate Matter

Thawed filters were halved for parallel analysis of labile and total particulate element concentrations following the digestion methods of Rauschenberg and Twining (2015). Half the membrane was leached using an acetic acid-hydroxylamine solution to solubilize labile elements (Berger et al., 2008), and the other half was digested with 4M HCl/4M HNO₃/4M

SOFEN ET AL. 3 of 23

Table 2

Cellular Elemental Contents and Size: Fe:C (μmol mol⁻¹, Least-Squares Geometric Means Controlling for Cell Size), Estimated Spherical Diameter (ESD, Range and Geometric Mean, μm), Number of Cells Analyzed (n), Community-Weighted C:P (C:P_{Org}, mol mol⁻¹ Calculated From 2019 BATS Community Composition (Lomas et al., 2022) and NASG Group-Specific Stoichiometry (Lomas et al., 2021))

			20 m				DCM			
Month	Fe:C	n	ESD range	ESD geom. mean	Fe:C	n	ESD range	ESD geom. mean	C:P _{org}	MLD (m)
March 2019	34 ± 7	25	0.8-5.9	1.9	43 ± 7	25	1.1–3.8	2.10	153	139 ± 9
May 2019	19 ± 4	16	0.9-5.0	1.97	31 ± 7	14	1.5-3.6	2.22	168	15 ± 2
August 2019	35 ± 8	15	0.8-3.9	1.40	36 ± 7	16	1.7-3.7	2.28	144	14 ± 2
November 2019	29 ± 5	27	0.8-5.2	1.99	46 ± 8	21	1.0-7.0	2.42	144	37 ± 7

Note. Mixed layer depth (MLD, m) is the average of three stations. Numbers in italics indicate 2021–2022 APS analysis. Numbers in italics indicate 2021–2022 APS analysis.

HF followed by 50% HNO₃/15% H₂O₂ (Ohnemus et al., 2014). The digest solutions were spiked with cesium as a recovery monitor. Reference materials (BCR414 and PACS-2) and process blanks (0.2- μ m filtered seawater passed through filters at sea) were digested alongside the samples. Replicate analyses of filter digests indicated method precision of 25% (Fe), 4% (P), and 21% (Al).

Digested samples were reconstituted in 2% HNO₃ for analysis by ICP-MS (Thermo Element2) using a medium resolution mode (Twining et al., 2023). Drift was monitored with ¹¹⁵In and concentrations were determined using external calibration curves. Limits of detection, process blanks, and recoveries of certified reference materials are shown in Table S3 in Supporting Information S1. When multiple isotopes were analyzed, the isotope with the lower detection limit was chosen: ²⁷Al, ³¹P, ⁴⁷Ti, ⁵⁷Fe, and ⁶⁸Zn (Twining et al., 2023).

2.4. Elemental Concentrations of Phytoplankton

Cellular metals were analyzed using synchrotron X-ray fluorescence spectroscopy (SXRF) following published methods (Twining et al., 2019) at the Advanced Photon Source, Argonne National Laboratory microprobe beamline 2-ID-E during three analytical runs: 3–8 March 2021 (2021-1; 74 cells from March, May, and November, 20 m depth), 23–28 June 2021 (2021-2; 76 cells from August, 20 m; March, May, August, DCM), and 18–23 November 2021 (2021-3; 21 cells from November, DCM; Twining & Sofen, 2023). Full details are provided in Supporting Information S1. Cell measurements were converted to an estimated spherical diameter, which ranged from 0.6 to 9.1 µm. Cellular elemental concentrations were normalized to cellular carbon contents, which were estimated from cell volume (Menden-Deuer & Lessard, 2000).

2.5. Calculation of Biogeochemical Fractions

The elemental concentrations of total and labile particulate matter were used in combination with phytoplankton cellular Fe quotas to parse the concentrations of lithogenic, biogenic, and authigenic PFe phases as a mass balance $(PFe_{Total} = PFe_{Lith} + PFe_{Bio} + PFe_{Auth})$. Two measurements of PFe_{Lith} were determined: (a) using a chemical digest and (b) using lithogenic end-members. PFe_{Labile} was sub-divided into biogenic and authigenic components by direct measurement of phytoplankton stoichiometry and phosphorus to yield PFe_{Bio} (Table 1). The residual of the mass balance was assigned to be PFe_{Auth} .

2.5.1. Biogenic PFe

The biogenic PFe fraction (PFe $_{Bio}$) was calculated from the geometric mean cellular quotas measured on each seasonal cruise:

$$PFe_{Bio} = Fe:C \times C:P_{Org} \times PP_{Labile}$$
(1)

We used depth-specific cellular Fe:C quotas (Fe:C) specific to each month determined using SXRF measurements of eukaryotic cells collected during these cruises, community-weighted C:P at BATS (C:P_{Org}), and PP_{Labile} measured from leached filters. PP_{Labile} includes the cellular and detrital material that make up the biogenic pool. Average measured surface and DCM Fe:C quotas are given in Table 2. An alternative calculation using only POC

SOFEN ET AL. 4 of 23

and Fe:C quotas is discussed in Text S6 and accompanying Figure S7 in Supporting Information S1. Quotas at depths between the surface and DCM were interpolated linearly.

For each cruise, we used a distinct $C:P_{Org}$ value calculated from group-specific particulate organic C:P stoichiometries (mean for North Atlantic Subtropical Gyre, Lomas et al., 2021) weighted by the community composition at BATS during these cruises (group-specific biomass integrated over 0–140 m, Lomas et al., 2022; Table S4 in Supporting Information S1). Although all PFe_{Bio} should be labile to the acetic acid-hydroxylamine leach, particle distribution is highly heterogeneous, and therefore PFe_{Bio} calculated from cellular stoichiometries was allowed to be up to 25% greater than PFe_{Labile}. In May, PFe_{Bio} exceeded PFe_{Labile} by more than 25% at four depths spread over two stations; in these samples, calculated PFe_{Bio} was assigned to be 1.25 times PFe_{Labile}.

2.5.2. Lithogenic PFe

Lithogenic PFe (PFe_{Lith}) was determined in two independent ways. First, it was defined as operationally refractory:

$$PFe_{Lith} = PFe_{Total} - PFe_{Labile}$$
 (2)

This will be referred to as the *total-leach method*. While it is impossible for labile material to exceed total material in the water column, heterogenous distribution of particles between the two halves of a given filter resulted in higher measurements of PFe_{Labile} than PFe_{Total} in 2% of measurements. In these cases, all material was assumed to be labile, hence $PFe_{Lith} = 0$.

Alternatively, PFe_{Lith} was estimated by using PAl as a proxy for lithogenic material:

$$PFe_{Lith} = PAl_{Total} \times Fe:Al_{Source}$$
(3)

This will be referred to as the *proxy method*. The *total-leach* PFe_{Lith} was compared to the *proxy* PFe_{Lith} as determined using several end members for the source Fe:Al ratio (Fe:Al_{Source}): (a) aerosols collected at Tudor Hill, Bermuda concurrently with our sampling (Sedwick et al., 2023), (b) upper continental crust (UCC; 0.23 mol Fe mol Al⁻¹, Rudnick & Gao, 2003), and (c) Saharan dust aerosol (0.42 mol Fe mol Al⁻¹, Shelley et al., 2015). The Tudor Hill aerosol sampling periods included the cruise periods and at least 1 week prior for a total of 13–22 days.

2.5.3. Authigenic PFe

Authigenic PFe (PFe_{Auth}) was defined by difference after removal of lithogenic and biogenic Fe:

$$PFe_{Auth} = PFe_{Total} - PFe_{Lith} - PFe_{Bio}$$
 (4)

In the *total-leach* method, that is, where PFe_{Lith} = PFe_{Refrac}, Equation 5 simplifies to

$$PFe_{Auth} = PFe_{Labile} - Fe_{Bio}$$
 (5)

Wherever the calculated PFe_{Bio} was greater than PFe_{Labile} (see Equation 2), PFe_{Auth} was set to 0.

2.5.4. Outlier Analysis in PFe Fractions

Marine particles are highly heterogeneous, and rare large particles captured on a filter can lead to substantially higher particle concentrations than is representative of mean conditions. Furthermore, when filters are split in half for parallel analyses of labile and total particulate matter, uneven particle distribution on the filter will affect PTM_{Labile}/PTM_{Total} ratios. To reduce heterogeneity due to sampling artifacts and focus on oceanographically relevant variability in particle concentrations, particle profiles for each cruise were inspected for consistency by comparing elemental concentrations and ratios within profiles from a single station and between bottles at similar depths from profiles at neighboring stations. Full details of data quality controls are presented in Text S1 in Supporting Information S1. Less than 5% of measurements were identified as outliers and replaced with a depth-weighted moving average (Table S5 in Supporting Information S1). Most outliers were in the upper 200 m, where the particle fraction is expected to be more dynamic.

2.6. Moving-Average b Values

Particle element concentrations (C) in the oceanic water column have been represented by a power law, $C(z) = C_0(z/z_0)^b$, where z is depth below z_0 surface, C_0 is concentration at the surface, and the sign of the exponent

SOFEN ET AL. 5 of 23

(b value) indicates whether particle flux is being attenuated (b < 0), accumulating (b > 0), or constant (b = 0) with depth (Lam et al., 2011; J. H. Martin et al., 1987). The magnitude of b indicates the strength of loss or accumulation of particles in the water column. Profile shapes of concentrations can be similarly assessed using a moving-average approach that captures the internal cycling of particulate TMs (PTMs) associated with different major phases (Boyd et al., 2017; Ohnemus et al., 2019; Saito et al., 2016). In general, biomass-associated elements like Cd and P have consistently negative moving-average b values as cellular material is remineralized during particle sinking. Elements that are associated with the refractory lithogenic fraction, such as Al and Ti, typically have moving-average b values near 0. Elements that are associated with multiple particulate phases, such as Fe, exhibit more complex structures in their moving-average b profiles that reflect the different phases involved and the processes that modify these phases at different depths (Ohnemus et al., 2019). Therefore, moving-average b profiles can be used to gain insight into the behavior of biological, lithogenic, and authigenic phases.

We calculated moving-average b values, as presented by Ohnemus et al. (2019), for each measured PFe fraction and PAI. Full details are provided in Text S5 and accompanying Figure S6 in Supporting Information S1. This approach allowed us to compare the magnitude of attenuation or accumulation of particle concentrations within different depth ranges, and thus evaluate the variability of processes with depth. Due to the high heterogeneity of particle measurements, some observations were not represented well by a local 3-point power law model, and fits with $r^2 < 0.5$ were excluded from further analyses. No evidence was found for significant differences between depth ranges for any PFe fraction (Kruskal-Wallis mean rank test, full results in Table S7 in Supporting Information S1), so the moving-average b values were aggregated into a single depth-weighted mean b for that cruise by weighting each moving-average b value by the depth range spanned by the three points used to calculate it.

2.7. Particulate Fe Phases in Other Regions

2.7.1. Sub-Antarctic Zone

In March 2018, the Southern Ocean Time Series (SOTS) study site was sampled five times by the RV *Investigator* (cruise IN2018_V02, Gilbert et al., 2022). Seawater (2.6–4 L) from 15 to 1,500 m was filtered onto 25 mm 0.4 μ m polyethersulfone membranes. As described in Section 2.3, labile particulate material was leached with an acetic acid-hydroxylamine solution and analyzed by ICP-MS (Twining, 2023a). To calculate PFe_{Bio} by Equation 1, PP_{Labile} concentrations were scaled by the mean Fe:C of phytoplankton collected from the surface mixed layer (6.5 \pm 1 μ mol Fe mol⁻¹ C; Sofen et al., 2022) and the Redfield ratio for C:P_{org} (Table S9 in Supporting Information S1). Measured C:P in this region was generally <100 and therefore, the Redfield ratio was chosen as a conservative upper limit of PFe_{Bio}. Any remaining PFe_{Labile} was assigned to be PFe_{Auth} following Equation 5. No total or refractory particulate measurements of this voyage were made.

2.7.2. California Upwelling Zone

The IrnBru cruise aboard the RV *Melville* (MV1405) in July 2014 sampled the California Current System at five stations covering three oceanographic environments: three offshore eddies (low Fe), a site of strong upwelling off Oregon, and a site of weak nearshore upwelling just north of San Francisco Bay (high N, Si, Fe, and chlorophyll a). Particles from approximately 2 L of water from 15 to 1,250 m were collected on 25 mm 0.4 μ m polyethersulfone membranes (Twining, 2016). Filters were leached first with acetic acid/hydroxylamine for labile material and subsequently digested with HCl/HNO₃/HF for remaining refractory material. Cellular iron content was measured in *Chaetoceros* cells from the weak upwelling site (Lampe et al., 2018). For other sites, Fe:C was calculated from DFe following the empirical relationship reported by Twining et al. (2021). At the weak nearshore upwelling station, concurrent measurements of surface particulate organic carbon (POC; Cohen et al., 2017) were compared to PP_{Labile} to calculate C:P_{org}. The calculated C:P_{org} (124) was close to the Redfield ratio and was used to calculate PFe_{Bio} following Equation 1 (Table S9 in Supporting Information S1). The remaining fractions were also defined as previously using the total-leach method following Equations 2 and 5.

2.7.3. Western Arctic

The Arctic GEOTRACES GN01 cruise in October 2015 traveled from Alaska through the Bering Strait to the North Pole via the Makarov Basin and returned through the Canada Basin. Half of the stations (13) occurred in off-shore, oligotrophic waters and half (14) were in near-shore, high-nutrient waters. An average of 6 L of water collected from 13 to 200 m was filtered through a 25 mm Supor 0.45 µm polyethersulfone membrane

SOFEN ET AL. 6 of 23

(GEOTRACES Intermediate Data Product Group, 2021). Filters were split into half for labile digestion using the acetic acid/hydroxylamine leach and the other half for total digestion using HCl/HNO₃/HF.

Cellular Fe quotas were measured at 4 near-shore and 3 off-shore stations (Twining, 2023b). The mean measured quotas were compared to quotas calculated from DFe (Twining et al., 2021). In areas of high DFe, the empirical relationship predicts unreasonably high quotas, so an upper limit of 300 µmol Fe mol⁻¹ C was used based on reported quotas in diatoms from Fe-replete conditions (Lampe et al., 2018; Sunda & Huntsman, 1995). Modeled and measured quotas diverged slightly close to the North Pole, but overall, the modeled quotas were in close agreement with measured quotas and were therefore used at other stations lacking quota measurements. Bulk C:P_{org}, calculated from PP and POC content of particles filtered by in situ pumps, was found to be slightly less than the Redfield ratio (106 mol mol⁻¹) and the Redfield ratio was used to calculate PFe_{Bio} following Equation 1 (Table S9 in Supporting Information S1). The remaining PFe fractions were calculated using the total-leach method following Equations 2 and 5.

2.7.4. Eastern South Pacific

The eastern tropical South Pacific was sampled along a coastal–open ocean gradient from October to December 2013 during the GEOTRACES GP16 (EPZT) cruise aboard the RV *Thomas G. Thompson*. Shelf stations (<250 km from shore) were characterized by high DFe (>0.2 nM), whereas open ocean stations (1,835-8,147 km from shore) were characterized by low DFe <0.2 nM and included both HNLC and oligotrophic regions. Seawater from 20 to 200 m was filtered onto 25 mm 0.4 \mu m polyethersulfone membranes. As described in Section 2.3, filters were split for parallel digestion and analysis by ICP-MS to determine total and labile particulate elemental contents (Twining et al., 2021). To calculate PFe_{Bio}, PP_{Labile} concentrations were scaled by empirically determined C:P of 86 (Lam et al., 2018) and station-specific geometric least-squares mean Fe:C of phytoplankton collected from the surface mixed layer at each station (Twining et al., 2021) (Table S9 in Supporting Information S1). Any remaining PFe_{Labile} was assigned to be PFe_{Auth} following Equation 5. PFe_{Lith} was defined using the total-leach method following Equation 2.

2.8. Ancillary Data

The four BAIT cruises occurred simultaneously with the regular BATS sampling campaigns. Core BATS program measurements, including macronutrient concentrations (phosphate, nitrate, nitrite), POC, PP, chlorophyll a (pigment 14), and biogenic silica (BSi), were accessed from the BATS data repository (http://bats.bios.edu/bats-data/).

2.9. Data Visualization and Statistical Analyses

Data visualization and statistical analyses were performed using the R programming language (R Core Team, 2022) in RStudio IDE (RStudio Team, 2021), including the use of tidyverse libraries (Wickham et al., 2019) and cowplot (Wilke, 2020).

3. Results

3.1. Oceanographic Context

At BATS, the mixed layer depth was nearly 140 m in March, shoaled to 14–15 m in May and August, and deepened to 37 ± 7 m in November (Table S2 in Supporting Information S1). The DCM was shallowest (65 ± 5 m) during the spring bloom in March, then deepened to 100–104 m in May and August, before shoaling to 78 ± 6 m by November (Table S2 in Supporting Information S1). The depth of the particle production zone (PPZ, defined as the surface down to the depth below the DCM where in situ chlorophyll fluorescence dropped to 10% of the fluorescence measured at 10 m, Owens et al., 2015) showed less seasonal variability, deepening from 140 ± 20 m in March to a maximum of 190 ± 20 m in August before reaching a minimum of 123 ± 3 m in November.

Macronutrient concentrations were low during the four cruises. Phosphate was below detection (0.01 μ M) from the surface through the DCM. Nitrate + nitrite was below detection (0.03 μ M) through the DCM in March and August. In May and November, nitrate + nitrite was below detection above the DCM and detectable at 0.21 and 0.45 μ mol kg⁻¹, respectively, at the DCM.

SOFEN ET AL. 7 of 23

19449224, 2023, 12, Downloaded from https://agupubs.onlinelibrary.wiley.com/doi/10.1029/2023GB007837, Wiley Online Library on [14/12/2023]. See the Terms and Conditions

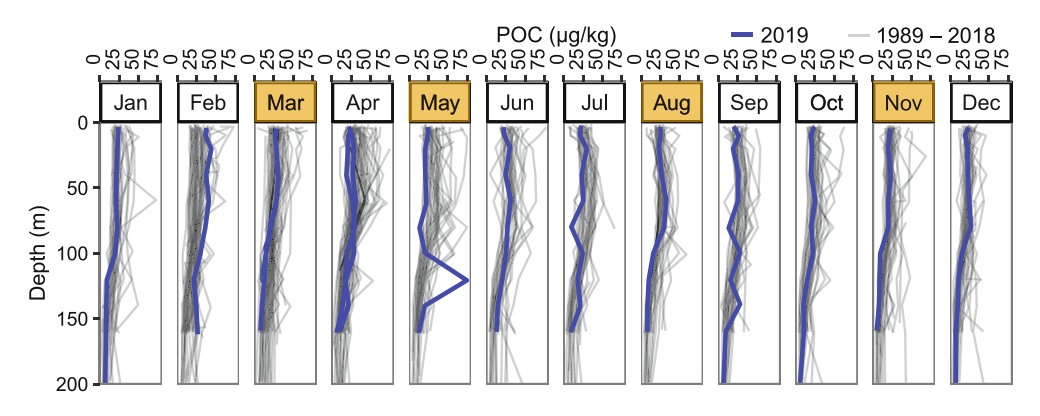


Figure 2. Particulate organic carbon (POC) in the upper 200 m during the study year (2019, blue lines) was consistent with the past 30 years on record (1989–2018, gray lines).

To assess how representative our single field sampling campaign was of climatological mean conditions, we compared three key biogeochemical parameters—POC (Figure 2), particulate organic phosphorus (POP; Figure S1a in Supporting Information S1) and chlorophyll-a (chlorophyll a, Figure S1b in Supporting Information S1)—measured for 2019 BATS cruises to the mean climatology from monthly BATS since 1988. The timing and magnitude of the 2019 spring bloom and summer stratification appeared representative of the long-term mean, although POP was lower than typical. The winter preceding the sampling season featured a positive NAO, which usually corresponds to a shallower mixed layer near Bermuda, and the winter-summer vertical mixing amplitude was small (Lomas et al., 2022).

3.2. Total Particulate Iron

Across seasons and depths, PFe_{Total} concentrations spanned two orders of magnitude, from 22 pM to 4.3 nM. The 5th and 95th percentiles of the bottle particle measurements were 120 pM and 1.7 nM (Figure 3a). Similar PFe_{Total} ranges have been measured previously in this region (Sherrell & Boyle, 1992; Twining, Rauschenberg, Morton, Ohnemus, & Lam, 2015). Profiles from August and November show local maxima at the surface, and minima at or below the DCM. Differences between stations were minor in all seasons except March, where the station nominally upstream of BATS had higher PFe_{Total} concentrations between 500 and 1,000 m than the other two stations. In other months, local maxima were observed around 800 m depth, corresponding to the OM (Figure S2 in Supporting Information S1). Average PFe_{Total} was significantly lower above the DCM than below in November (F(1,4) = 36.4, p = 0.004, Analysis of Variance, ANOVA) but did not vary between depth intervals in other seasons. Surface concentrations were significantly higher in May and November than in March (F(1,9) = 5.2, p = 0.05, ANOVA). Across seasons, the average PFe_{Total} concentration \pm one standard deviation (SD) measured in the upper 1,700 m was 0.9 ± 0.1 nM. Concentrations were more variable above the DCM than below (Figure S2a in Supporting Information S1).

Net PFe_{Total} accumulation below the PPZ was observed in May, August, and November (Figure 4a). Between 33% and 80% of observations fit a local 3-point power law model ($r^2 > 0.5$, Table S6 in Supporting Information S1). The poor fit to a power law suggests that many competing processes contribute to PFe_{Total} concentrations throughout the water column, and different processes may dominate at different depths such that a single power law cannot describe the net effect even over a small depth interval. Accumulation of PFe_{Total} was strongest following the spring bloom ($b_{\text{May}} = 0.9 \pm 0.3$, mean ± 1 standard error). Preceding the spring bloom, there was weak net attenuation in March. DFe profiles (Sedwick et al., 2023) show a consistent increase in concentration with depth across seasons, with mean moving-average b values from 0.50 ± 0.2 (August and November) to 0.8 ± 0.1 (March). However, the greatest depth increase of DFe occurred during March when particle accumulation was lowest. The accumulation of PFe_{Total} with depth shows similar median moving-average b values to those reported for a transect of the South Pacific (Ohnemus et al., 2019), although data in the BATS region was too sparse to confidently observe depth variations seen in the South Pacific.

SOFEN ET AL. 8 of 23

19449224, 2023, 1 2, Downloaded from https://agupubs.onlinelibary.wiley.com/doi/10.1029/2023GB007837, Wiley Online Library on [14/12/2023]. See the Terms and Conditions (https://onlinelibary.wiley.com/terms-and-conditions) on Wiley Online Library for rules of use; OA articles are governed by the applicable Creative Commons Licenses

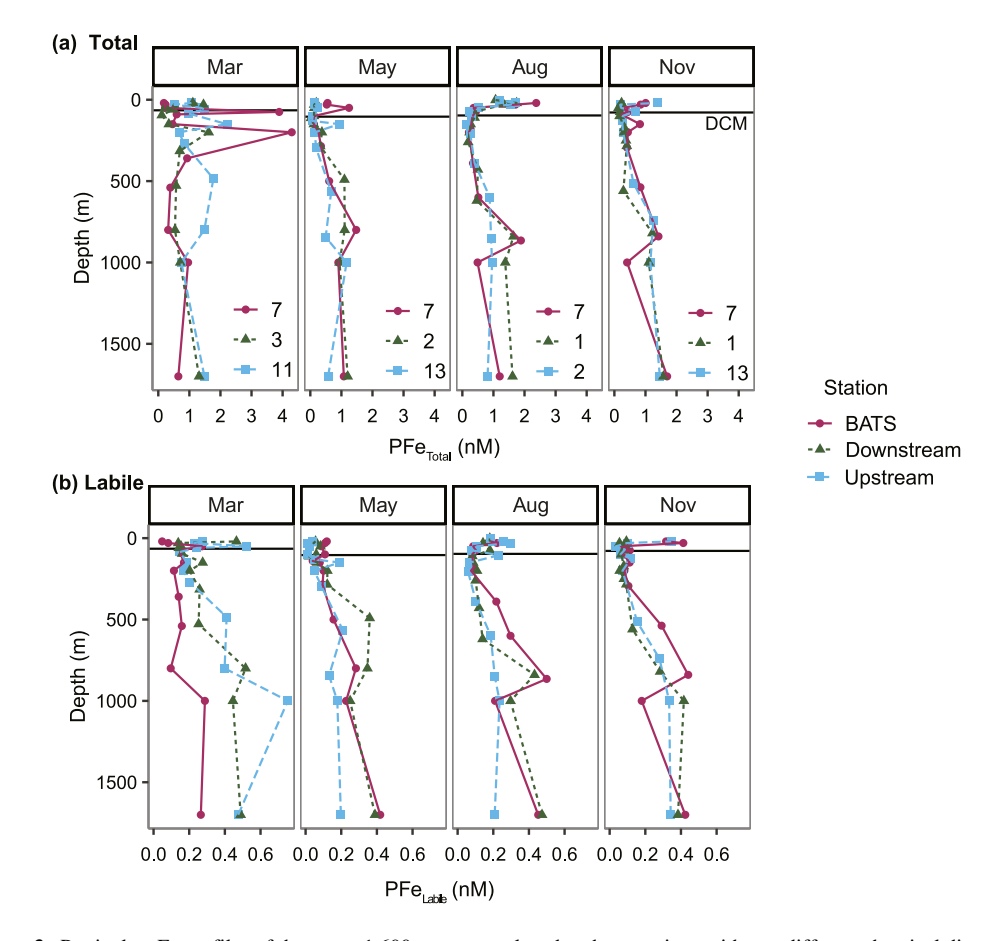


Figure 3. Particulate Fe profiles of the upper 1,600 m were analyzed at three stations with two different chemical digests to measured Total (a) and Labile (b) Fe.

3.3. Labile Particulate Iron

Across seasons and depths in the BATS region, PFe_{Labile} concentrations also spanned two orders of magnitude, 8–750 pM Fe. The 5th and 95th percentiles of bottle measurements were 45 and 460 pM (Figure 3b). Depth profiles were similar to the PFe_{Total} profiles: concentrations increased below the DCM, with local maxima around

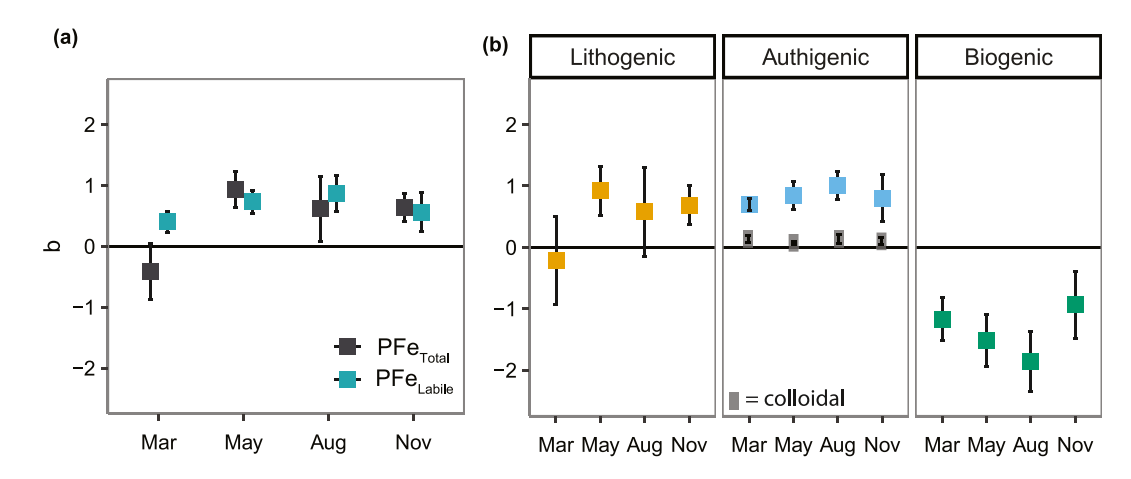


Figure 4. Particle attenuation (b < 0) and accumulation (b > 0) of total (a), labile (a), lithogenic (b), authigenic (blue squares) and colloidal (gray rectangles) (b), and biogenic (b) Fe between the base of the particle production zone (variable with season, 96–230 m) and 1,700 m. Mean \pm 1 SE of 3-point moving b values with $r^2 > 0.5$, weighted by the depth range.

SOFEN ET AL. 9 of 23

the OM (Figure S2 in Supporting Information S1). The lowest surface PFe_{Labile} concentrations were observed in May and the highest in November, demonstrating a disconnect with seasonal DFe concentrations (Sedwick et al., 2023). Average PFe_{Labile} concentrations were 80%–250% higher below the DCM than above it in May, August, and November (ANOVA: May F(1,2) = 36, p = 0.026; August F(1,4) = 9, p = 0.039; F(1,4) = 27, p = 0.007), but concentrations were not significantly different between seasons within each depth interval. Despite these depth differences in absolute concentration, the fractional labile portion of PFe_{Total} (33 \pm 20%) was not different above and below the DCM. The observed fractional labilities were comparable to earlier measurements in the region (20%, Rauschenberg & Twining, 2015).

High surface concentrations of PFe_{Labile} in November resulted in strong attenuation of the profiles through 200 m depth ($b = -1.1 \pm 0.1$, mean \pm SE, Figure 4a). The moving-average b values for PFe_{Labile} for shallower depths and all depths for the other three cruises were not significantly different from one another (p > 0.1, ANOVA b vs. depth bin) and were positive, indicating the accumulation of PFe_{Labile} with depth (0.4 ± 0.2 March, 0.7 ± 0.2 May, 0.9 ± 0.3 August, 0.6 ± 0.3 November). Complex cycling involving PFe_{Labile} is implied by the high number of observations (20%–50%) that did not fit a local 3-point power law model ($r^2 < 0.5$, Table S6 in Supporting Information S1).

3.4. Refractory and Lithogenic Particulate Iron

PFe_{Lith}, operationally defined as PFe_{Refrac} as measured using the *total-leach method*, ranged from 0 to 4.2 nM across all seasons and depths. The 5th and 95th percentiles of measurements were 150 and 790 pM (Figure 5a, as PFe_{Lith}). The highest concentrations were observed at the surface in August, coincident with the period of maximum Saharan dust deposition (Sedwick et al., 2023). A local maximum PFe_{Refrac} around the OM (Figure S2 in Supporting Information S1) was apparent in May, August, and November but less clear in March when PFe_{Refrac} exceeded 3 nM at two depths from the BATS station (75 and 200 m). Such a feature could arise from lateral inputs (Hwang, Manganini, et al., 2009; Hwang, Montluçon, & Eglinton, 2009) or from vertical propagation of the annual dust signal (Ohnemus & Lam, 2015). The first is unlikely, as beam transmissometry profiles (Figure S3 in Supporting Information S1) do not indicate locally elevated particle loads. The vertical propagation of the dust signal may or may not produce a transmissometry signal. Average PFe_{Refrac} was higher below the DCM than above it in November (F(1,4) = 8.3, p = 0.045, ANOVA), but in no month was there a significant difference between depths in the percentage of PFe_{Total} that was refractory ($70 \pm 10\%$, mean \pm one SD across seasons and depth intervals, Figure S4b in Supporting Information S1).

Despite similar average concentrations above and below the DCM, power law analysis indicated that PFe_{Total} accumulation was driven by net refractory particle accumulation following the spring bloom over the 40%–80% of observations that fit a 3-point power law (Figure 4b). Like PFe_{Total}, PFe_{Refrac} showed weak attenuation in March ($b = -0.2 \pm 0.4$) followed by strong accumulation with depth beginning in the late spring ($b_{May} = 0.9 \pm 0.4$) and persisting through the summer and fall ($b_{Aug} = 0.6 \pm 0.7$, $b_{Nov} = 0.7 \pm 0.3$).

For the proxy method, lithogenic end member ratios were compared. Molar ratios of PFe_{Refrac}:PAI_{Total} in water column particles (Fe:Al = 0.21 ± 0.03 and 0.19 ± 0.04 , respectively, regression slope \pm one standard error) were similar to the UCC reference ratio (0.23 mol mol⁻¹, Rudnick & Gao, 2003) in March and May. Ratios observed in August and November were higher $(0.30 \pm 0.01 \text{ and } 0.27 \pm 0.04, \text{ respectively}; \text{ Figure 6b})$, intermediate between UCC and North African mineral aerosol reference ratios (0.37, Shelley et al., 2015). Atmospheric deposition collected at Tudor Hill concurrent to the cruises (Sedwick et al., 2023) showed Fe:Al ratios similar to marine particles: on average 64%-95% of marine Fe:Al, with the largest discrepancy in November (Figure 6b). The excellent regression fit of the individual elements ($r^2 = 0.95$) in August indicates greater uniformity in particle composition, consistent with higher dust deposition during this season. In contrast, other months exhibited weaker coupling of Fe and Al, with plots of PFe_{Refrac} versus PAl_{Total} suggesting variability in mineral composition that might reflect different lithogenic sources (Figure 6a). Potential diatom contribution to PAI was estimated from the BATS climatology of biogenic Si (BSi, see Methods in Supporting Information S1): diatoms appeared to account for a maximum of 1%-3% of PAI_{Total} in the upper 250 m across all seasons. This would result in 1%-3% higher Fe:Al ratios, still within the range of UCC and aerosol reference ratios. In another step to evaluate the proxy and total-leach methods, accumulation of PFe_{Refrac} and the lithogenic tracer PAl_{Total} with depth (moving-average bvalues) were comparable in all months (Figure 6c).

SOFEN ET AL. 10 of 23

19449224, 2023, 12, Downloaded from https://agupubs.onlinelibrary.wiley.com/doi/10.10.199/2023GB007837, Wiley Online Library on [14/12/2023]. See the Terms and Conditions (https://onlinelibrary.wiley.com/terms-and-conditions) on Wiley Online Library for rules of use; OA articles are governed by the applicable Creative Commons Licensea

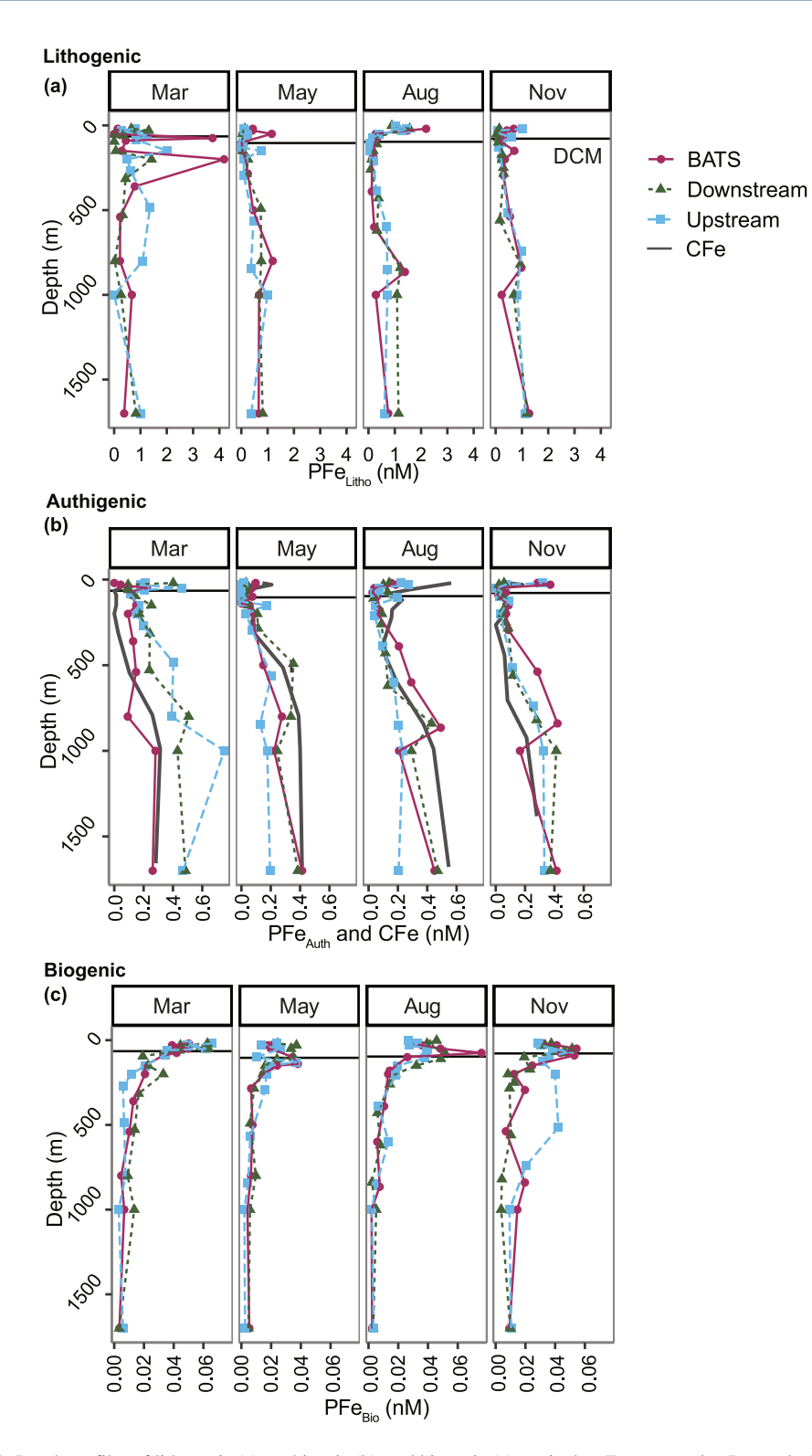


Figure 5. Depth profiles of lithogenic (a), authigenic (b), and biogenic (c) particulate Fe measured at Bermuda Atlantic Time-series Study (BATS) and nearby spatial stations. Station labels for profiles are as in Figure 3. Colloidal Fe (CFe) in (b) was measured at the BATS site (Tagliabue et al., 2023).

SOFEN ET AL. 11 of 23

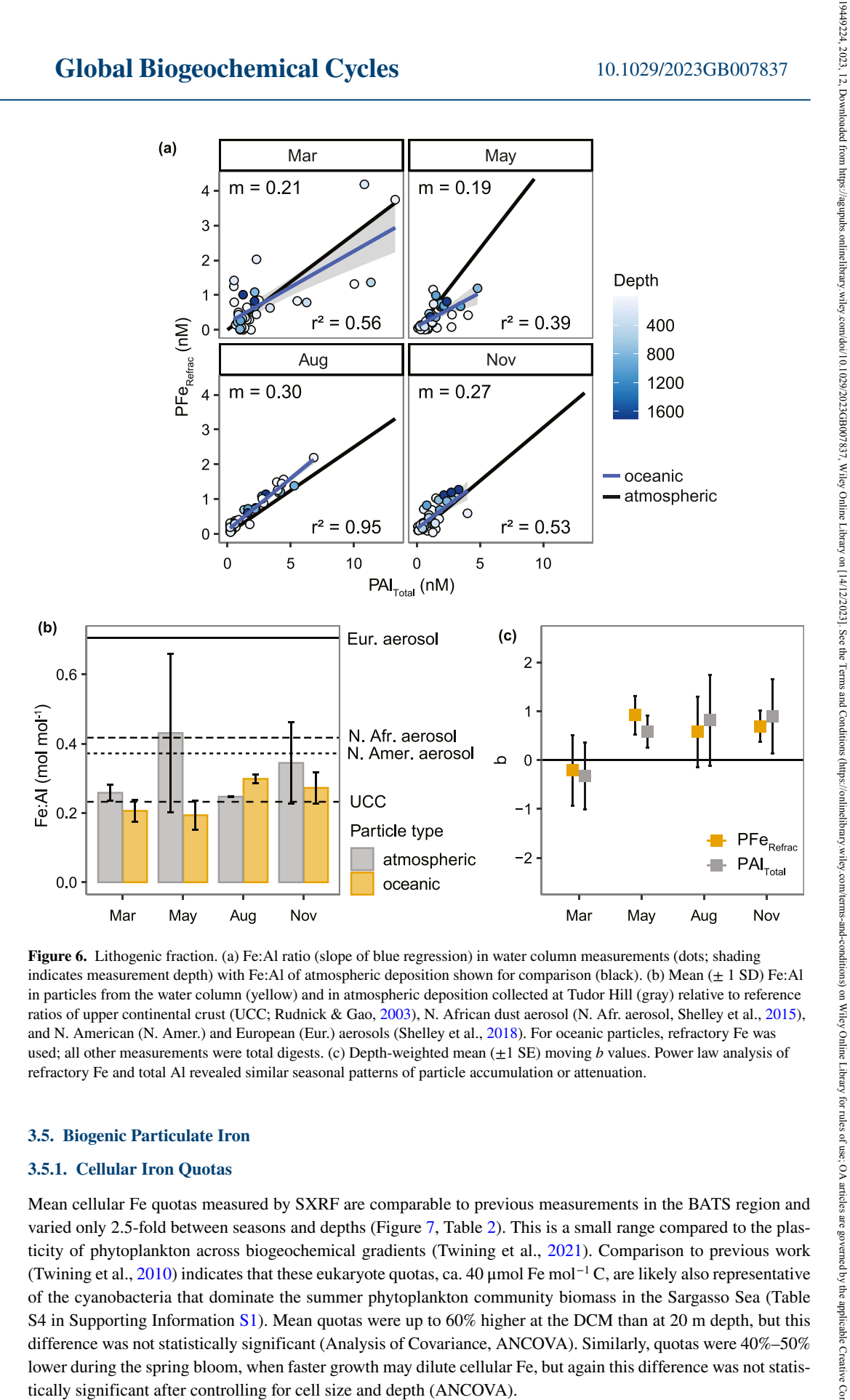


Figure 6. Lithogenic fraction. (a) Fe:Al ratio (slope of blue regression) in water column measurements (dots; shading indicates measurement depth) with Fe:Al of atmospheric deposition shown for comparison (black). (b) Mean (± 1 SD) Fe:Al in particles from the water column (yellow) and in atmospheric deposition collected at Tudor Hill (gray) relative to reference ratios of upper continental crust (UCC; Rudnick & Gao, 2003), N. African dust aerosol (N. Afr. aerosol, Shelley et al., 2015), and N. American (N. Amer.) and European (Eur.) aerosols (Shelley et al., 2018). For oceanic particles, refractory Fe was used; all other measurements were total digests. (c) Depth-weighted mean (±1 SE) moving b values. Power law analysis of refractory Fe and total Al revealed similar seasonal patterns of particle accumulation or attenuation.

3.5. Biogenic Particulate Iron

3.5.1. Cellular Iron Quotas

Mean cellular Fe quotas measured by SXRF are comparable to previous measurements in the BATS region and varied only 2.5-fold between seasons and depths (Figure 7, Table 2). This is a small range compared to the plasticity of phytoplankton across biogeochemical gradients (Twining et al., 2021). Comparison to previous work (Twining et al., 2010) indicates that these eukaryote quotas, ca. 40 µmol Fe mol⁻¹ C, are likely also representative of the cyanobacteria that dominate the summer phytoplankton community biomass in the Sargasso Sea (Table S4 in Supporting Information S1). Mean quotas were up to 60% higher at the DCM than at 20 m depth, but this difference was not statistically significant (Analysis of Covariance, ANCOVA). Similarly, quotas were 40%-50% lower during the spring bloom, when faster growth may dilute cellular Fe, but again this difference was not statistically significant after controlling for cell size and depth (ANCOVA).

SOFEN ET AL. 12 of 23

9449224, 2023, 12, Downloaded from

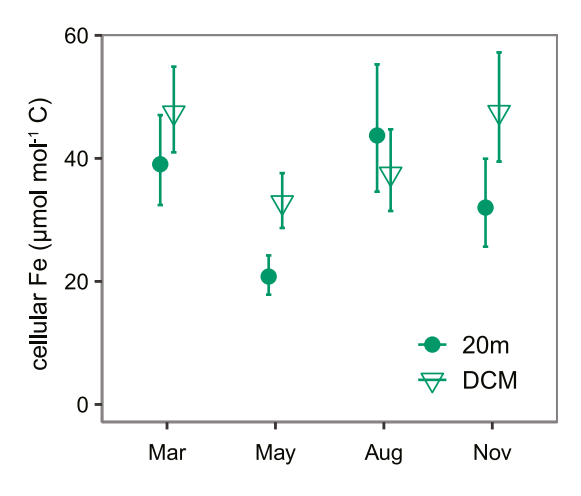


Figure 7. Carbon-normalized cellular Fe quotas (mean \pm 1 SE) of phytoplankton collected at Bermuda Atlantic Time-series Study from the surface (filled circle) and deep chlorophyll maximum (DCM) (open triangle).

3.5.2. Labile Particulate Phosphorus

Nearly all particulate phosphorus was associated with biogenic particles in the BATS region. The lithogenic contribution to PP_{Total} was estimated from the measured PAl_{Total} and an end member $P:Al = 0.0076 \text{ mol mol}^{-1}$ (Taylor & McLennan, 1995). This PP_{Litho} fraction was negligible compared to PP_{Labile}, with the inventory never exceeding 1.2% of the PP_{Labile} inventory. However, there was a significant fraction (median = 16%) of PP that was not digested by the acetic acid leach. Previous studies have also reported ca. 15%-20% PP (Twining et al., 2019, 2021) or as much as 60% PP (Al-Hashem et al., 2022) that is not accessed by the acetic acid/ hydroxylamine leach. This suggests a widely prevalent non-lithogenic PP_{Refrac} source in the ocean. The chemical nature of this refractory P is unclear but may include polyphosphates that are not labile to the acetic acid-hydroxylamine leach (P. J. H. Martin et al., 2014) and/or aged biogenic material (Al-Hashem et al., 2022). No significant differences were found between average PP_{Labile} across seasons within each depth interval (ANOVA, p > 0.1).

3.5.3. Biogenic Particulate Iron

 PFe_{Bio} in the BATS region comprised 5%-15% of the total particulate inventory and 23%-40% of labile particulate iron above the DCM and only about

1% of PFe_{Total} below the DCM (Figure S5 in Supporting Information S1). Average concentrations did not differ significantly between cruises (ANOVA, p > 0.1); averaged over all four seasons, PFe_{Bio} was 45 \pm 13 pM above the DCM and 10 ± 5 pM in deeper waters (Figure 5c, Figure S4d in Supporting Information S1). Considering the 2.5-fold range of quotas measured, and the approximately 40% variability in seasonal C:P values for the region, the uncertainty in these inventories may be as much as 3.5-fold.

As expected, PFe_{Bio} was the only PFe fraction to exhibit net attenuation with depth (Figure 4b). Attenuation was strongest in August ($b = -1.9 \pm 0.5$) and weakest in November ($b = -0.9 \pm 0.5$). Only 40%–80% of the 3-point fits conformed to a power law model ($r^2 > 0.5$, Table S6 in Supporting Information S1), a surprising result given that PP can typically be modeled by a single power law (Ohnemus et al., 2019). This underscores that marine particles are highly dynamic, such that data aggregation to a higher level is useful to pull out trends.

3.6. Authigenic Particulate Iron

Across seasons and depths in the BATS region, PFe_{Auth} concentrations spanned 0–4.18 nM Fe. The 5th and 95th percentiles of measurements were 0.04 and 1.4 nM, a larger dynamic range than the other fractions (Figure 5b). The depth profiles were similar in shape to the PFe_{Labile} profiles, with strong increases below the DCM and slightly elevated concentrations around the OM (Figure S2 in Supporting Information S1). Concentrations were not significantly different between seasons (F(1,19) = 2.8, p > 0.1, ANCOVA effect of cruise after controlling for depth). PFe_{Auth} was 1.3–2.0 times higher below the DCM than above (280 ± 80 and 110 ± 70 pM, respectively; F(1,19) = 64.4, p = 1.6e-5, ANCOVA effect of depth after controlling for the cruise, Figure S4c in Supporting Information S1) and comprised a significantly higher proportion of the PFe_{Labile} pool below the DCM (94%–97%) than above it (60%–76%) for every month except May (ANOVAs: March F(1,4) = 25, p = 0.008; August F(1,4) = 43, p = 0.003; November F(1,4) = 16, p = 0.015, Figure S5 in Supporting Information S1). To consider whether the magnitude of this fraction results from uncertainty in PFe_{Bio}, the maximum possible PFe_{Bio} pool (see Section 3.4.3) can be compared to the PFe_{Labile} pool. This 3.5-fold increase in PFe_{Bio} can account for all PFe_{Labile} at the surface, but below the DCM, a sizable pool of PFe_{Auth} would still remain, ca. 245 pM, indicating that this fraction is not an artifact of the method by which it was calculated.

PFe_{Auth} accumulated with depth in all seasons except November ($b = 0.7 \pm 0.1$ March, 0.8 ± 0.2 May, 1.0 ± 0.2 August) when high surface concentrations drove large negative moving-average b values above 200 m ($b = -1.5 \pm 0.4$ above 200 m, 0.8 ± 0.4 below 200 m; Figure 4b). There was high variability in the fit skill of

SOFEN ET AL. 13 of 23

19449224, 2023, 12, Downloaded from https://agupubs.onlinelibrary.wiley.com/doi/10.1029/2023GB007837, Wiley Online Library on [14/12/2023]. See the Terms and Conditions

(https://onlinelibrary.wiley.com/terms-and-conditions) on Wiley Online Library for rules of use; OA articles are governed by the applicable Creative Commons License

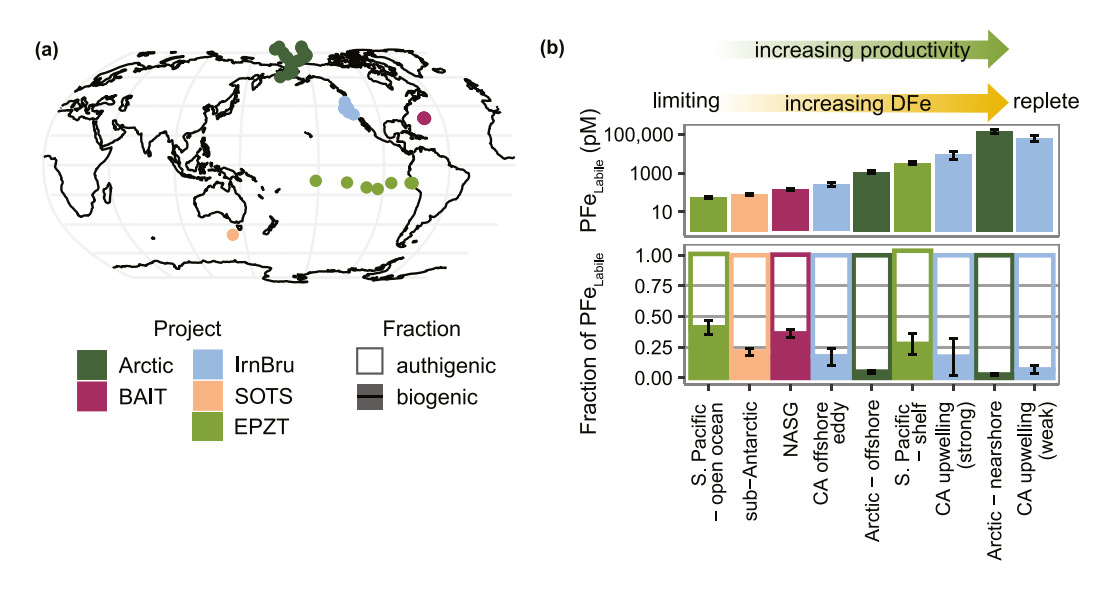


Figure 8. Partitioning of labile PFe into biogenic and authigenic fractions across environmental conditions. (a) Sampling sites in four ocean basins. (b) Fraction of labile PFe in the upper 200 m that is biogenic (filled bar) and authigenic (unfilled bar).

the power law, with 17%-100% of observations fitting a 3-point regression with $r^2 > 0.5$ (Table S6 in Supporting Information S1).

3.7. Colloidal Iron

Colloid concentrations (Figure 5b) were estimated from the difference between dissolved ($<0.2 \mu m$) and soluble ($<0.02 \mu m$) Fe concentrations (Tagliabue et al., 2023). The log-transformed concentration profiles were used to calculate the moving-average b values by fitting 3-point linear regressions. These regression fits were generally better (i.e., higher r^2) than for PFe phases. All moving-average b values were close to 0 and were averaged with depth weighting across depths for a single moving-average b value for each season.

3.8. Comparison With Other Regions

PFe fractions were estimated for other regions of the ocean using existing data to evaluate whether the trends we have documented in the BATS region are common to other biogeochemically distinct oceanic environments (Figure 8, Table 3). The SOTS station represents sub-Antarctic waters and was sampled in austral fall. The IrnBru cruise sampled coastal California Current waters, with stations spanning nearshore (10 km) waters with high DFe

Table 3PFe Fractions and DFe in Sub-Antarctic, Western Arctic, and Coastal California (CA) Upwelling Zone Regions Above 200 m (nM, Geometric Mean ± 1 Standard Error of n Samples)

Location	n	PFe_{Total}	PFe_{Lith}	PFe_{Auth}	PFe_{Bio}	DFe
Sub-Antarctic	31	N/A	N/A	0.057 ± 0.006	0.011 ± 0.001	0.27 ± 0.02
Arctic—offshore	64	1.5 ± 0.2	0.7 ± 0.1	0.7 ± 0.1	0.016 ± 0.002	0.57 ± 0.06
Arctic—nearshore	42	41 ± 19	15 ± 11	16 ± 7	0.18 ± 0.06	1.5 ± 0.4
CA—offshore eddy	11	0.7 ± 0.3	0.5 ± 0.2	0.14 ± 0.05	0.013 ± 0.004	0.6 ± 0.1
CA—strong upwelling	4	16 ± 13	14 ± 8	6 ± 5	0.13 ± 0.06	1.2 ± 0.6
CA—weak upwelling	6	164 ± 115	160 ± 90	40 ± 20	1.1 ± 0.1	9 ± 2
Equatorial Pacific—open ocean	24	0.14 ± 0.01	0.08 ± 0.01	0.036 ± 0.005	0.016 ± 0.002	0.09 ± 0.08
Equatorial Pacific—shelf	27	2.5 ± 0.6	0.8 ± 0.1	2.0 ± 0.5	0.070 ± 0.008	0.8 ± 0.6

Note. PFe_{Lith} was determined using the total-leach method.

SOFEN ET AL. 14 of 23

and also offshore (70–270 km) waters with lower DFe concentrations. South Pacific and Arctic GEOTRACES stations similarly spanned a range of DFe conditions, potential shelf inputs, and phytoplankton community compositions. Overall, across these diverse environments, PFe_{Auth} was consistently observed to dominate and PFe_{Labile}.

PFe_{Total} measurements are not available for the SOTS cruise. However, the labile fraction was $79 \pm 3\%$ authigenic and $21 \pm 3\%$ biogenic averaged across all depths above 200 m and sampling casts (Figure 8b, Table 3). At the SOTS station, biomass during austral fall is typically high and dominated by diatoms, with nanoflagellates also abundant (Eriksen et al., 2018).

In the California Upwelling Zone, PFe_{Total} spanned three orders of magnitude between the three station types, but PFe_{Labile} accounted for 20%-25% of PFe_{Total} across all station types. Individual fractions followed similar trends: concentrations were highest at the weak upwelling station, intermediate at the strong upwelling station, and lowest at the three eddy stations (Figure 8b, Table 3). PFe_{Labile} was dominated by PFe_{Auth}, with slightly more PFe_{Auth} at the high-Fe site (93 \pm 3%) than at the strong upwelling (83 \pm 15%) and eddy sites (83 \pm 7%).

In the Arctic, PFe $_{Total}$ concentrations were 26 times higher near-shore than off-shore, but in both regions PFe $_{Labile}$ accounted for 46%–52% of PFe $_{Total}$. Proportions of each fraction were also similar between the two regions despite order-of-magnitude higher concentrations at the near-shore stations than at the off-shore stations (Figure 8b, Table 3), and PFe $_{Labile}$ was dominated by PFe $_{Auth}$ throughout (95%–97% in both regions).

In the South Pacific Ocean, PFe_{Total} concentrations were 18 times higher near shore than off shore, but the fraction of this that was labile was only slightly higher on the shelf ($60 \pm 3\%$ near-shore, $46 \pm 3\%$ off-shore). The labile fraction consisted of a higher proportion of PFe_{Auth} near shore ($76 \pm 7\%$) than off shore ($60 \pm 5\%$, Figure 8b, Table 3).

4. Discussion

Our seasonal study in the BATS region has revealed that most (60%–97%) of the chemically labile PFe pool was abiotic, a finding replicated at other oceanic sites that represent a wide range of biological productivity.

4.1. Biogenic Fe Is a Small Fraction of Labile PFe

Measurement of the authigenic fraction requires first constraining the contribution of PFe_{Bio} to PFe_{Labile} . This has typically been done using a single global mean Fe:P or Fe:C ratio for all biomass and scaling to particulate P or C (Black et al., 2020; Marsay et al., 2017). However, this approach ignores the significant variability in cellular Fe contents that occurs between regions and bloom phases (up to 40-fold, King et al., 2012; Twining et al., 2021), and thus introduces significant uncertainties. Here, we directly measured the labile fraction and cellular Fe:C stoichiometry to better constrain the biogenic fraction and more accurately assess authigenic Fe. The acetic acid/hydroxylamine leach solubilizes metals associated with cells and oxyhydroxides (Berger et al., 2008). In our samples, the measured labile fraction was almost always much greater than the estimate of PFe_{Bio} calculated from concurrently measured cell stoichiometry, PP_{Labile} , and season-specific community C:P ratios. In 85% of the 146 discrete particle samples, PFe_{Bio} constituted less than half of the PFe_{Labile} , similar to previous findings from BATS where PFe_{Bio} accounted for 30% of PFe_{Labile} (Twining, Rauschenberg, Morton, & Vogt, 2015).

Iron cell quotas did not vary significantly with season or depth, although slightly higher quotas were observed in samples from the DCM than from 20 m. Such a depth effect has been proposed as due to photo-acclimation (Hopkinson & Barbeau, 2008; Sunda & Huntsman, 1997), and indeed, chl/POC ratios in all months were 3–11 times higher around the DCM than the surface despite equal or lower DFe at the DCM (Sedwick et al., 2023). The lack of significant differences in station-aggregated Fe:C quotas at the surface and DCM is consistent with previous work across the North Atlantic (Twining, Rauschenberg, Morton, Ohnemus, & Lam, 2015) as well as with a macronutrient-limited rather than Fe-limited community (Twining et al., 2021). Notably, the eukaryotes measured in this study constitute 26%–46% of the phytoplankton carbon pool (Table S5 in Supporting Information S1). Although previous work indicates similar Fe requirements in cyanobacteria in this region, future work to characterize seasonal variability in Fe contents of *Synechococcus* and *Prochlorococcus* could improve our understanding of these communities and the estimates of PFe_{Rio}.

SOFEN ET AL. 15 of 23

The apparent seasonal changes in PFe_{Bio} profiles are consistent with seasonal phytoplankton shifts in the BATS region. The mixed layer shoaled from 139 ± 9 m in March to 14 ± 1 m in May and August. As the water column stratified and macronutrients became limited at the surface, biomass maxima are typically found deeper (Hahn-Woernle et al., 2014). Such a trend is evident in the long-term BATS record of POC and chlorophyll and in POC data for 2019, although the chlorophyll maximum in August 2019 was in fact shallower than in March 2019. Maximum PFe_{Bio} also shifted from the surface in March to the subsurface in August. In November at SS13, nominally upstream of the BATS station, PFe_{Bio} appeared elevated throughout the upper water column to 500 m, a trend not observed in any other PFe fraction, PP_{Total}, or transmissometry, a proxy for POC (Figure S3 in Supporting Information S1). This feature was observed in the percent labile PP and PFe, suggesting that it is an artifact of the digestion procedure for that station. Because both labile fractions were equally affected, the percent authigenic could still be assessed.

Our estimate of PFe_{Bio} from PP_{Labile} is likely a lower bound on PFe_{Bio} because it assumes that (a) Fe and P remineralization are coupled and (b) all biogenic PFe is associated with phytoplankton. Regarding the first point, elements can cycle at different rates (Marsay & Achterberg, 2021; Rafter et al., 2017; Twining et al., 2014), especially in subtropical waters where P is scarce. Our calculation of PFe_{Bio} assumes that Fe:P ratios in surface cellular material are representative of fecal and detrital particles, which are also components of PP_{Labile} . The vertical variability of Fe:P in non-cellular labile particles may contribute to some uncertainty in the calculation of PFe_{Bio}. The apparent variability in moving-average b values from -1.0 to -1.9 suggests that some seasonal differences in P remineralization are present; this range is only slightly greater than the variability of North Pacific Subtropical Gyre PP fit values of ca. -0.88 ± 0.48 (Boyd et al., 2017). Moreover, the initial release of Fe and P together from biogenic particles may become decoupled subsequently, presumably due to abiotic removal of Fe (Hollister et al., 2020). Turning to the second point, other plankton groups likely contribute non-negligibly to PFe_{Bio}. Heterotrophic plankton also incorporate Fe, and thus our PFe_{Bio} estimate is likely conservative if these groups have higher Fe/C quotas and an overestimate if these groups have lower Fe/C quotas. In previous studies at the FeCycle study site in the Southern Ocean and in waters on the Kerguelen Plateau, zooplankton and heterotrophic bacteria together accounted for 40%-50% of biogenic Fe compared with cyanobacteria and diatoms (Boyd et al., 2015). These plankton groups also likely contribute significantly to the PFe_{Bio} pool at BATS, where heterotrophic bacteria comprise 10%–18% of particulate C and 20%–37% of PP (Martiny et al., 2013). A significant zooplankton Fe pool may move PFe_{Bio} from the surface to the subsurface through vertical migration (Steinberg & Landry, 2017), also "repackage" PFe in a more labile form (Schmidt et al., 2016). However, it is notable that these factors are most important to calculations of the surface and near-surface PFe pools, where our PFe_{Bio} calculations approached PFe_{Labile} ; at greater depths PFe_{Bio} is a near-negligible component of PFe_{Labile}

Our approach highlights the need for better estimates of PFe_{Bio}, and the importance of an authigenic PFe fraction. Taxon-specific cell quotas and community composition can refine PP-based estimates of PFe_{Bio}. However, the decoupling of Fe and P remineralization remains an issue in any approach using Equation 1, so additional methods to differentiating cellular Fe from chemically labile Fe are needed.

4.2. Authigenic Iron Is the Major Component of the Labile Fraction

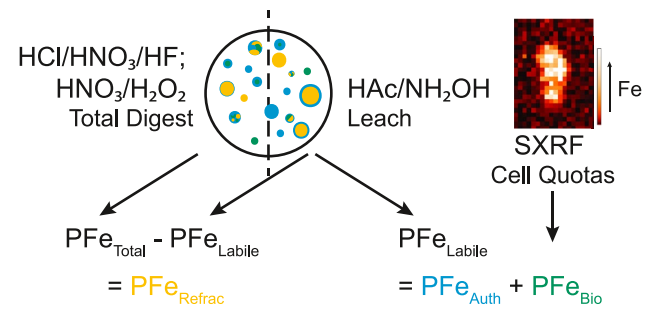
In the BATS region, PFe_{Auth} is the major component of PFe_{Labile} and a notable fraction of PFe_{Total}. Refractory and cellular PFe account for 70%–80% of PFe_{Total}. PFe_{Labile} is consistently 30% of PFe_{Total}, and even if our stoichiometry-based PFe_{Bio} estimate is as much as 50% too low (see Section 4.3), there must be a sizable pool of PFe that is abiotic but chemically labile. Similar estimates were reported in a recent study that assumed a lower bound biogenic particle stoichiometry of 0.005 mol Fe mol⁻¹ P or a locally derived Fe:P ratio where available, resulting in PFe_{Auth} concentrations of up to 44% of PFe_{Total} and 85% of PFe_{Labile} (Black et al., 2020). This adds to a growing body of research that finds that authigenic material dominates non-lithogenic material (e.g., Marsay et al., 2018; Xiang & Lam, 2020). This is an important contrast with early analyses of PTMs that assumed that all non-lithogenic material was biogenic, likely leading to overestimates of cellular elemental quotas (Bruland et al., 1991; J. H. Martin & Knauer, 1973). Allowing for the existence of an authigenic phase brings bulk particle measurements into better agreement with cellular stoichiometry measurements.

Given the size of the PFe_{Auth} pool and the role of particles in transporting TMs, understanding the formation and fate of authigenic material is critical to understanding the ocean Fe cycle (Tagliabue et al., 2019, 2023). A local minimum in PFe_{Auth} around the DCM suggests that the material may be solubilized at the DFe minimum or potentially removed from the surface via packaging into larger, faster-sinking particles. Likely mechanisms of PFe_{Auth} formation include aggregation of smaller colloids of Fe minerals (CFe) into larger PFe_{Auth}

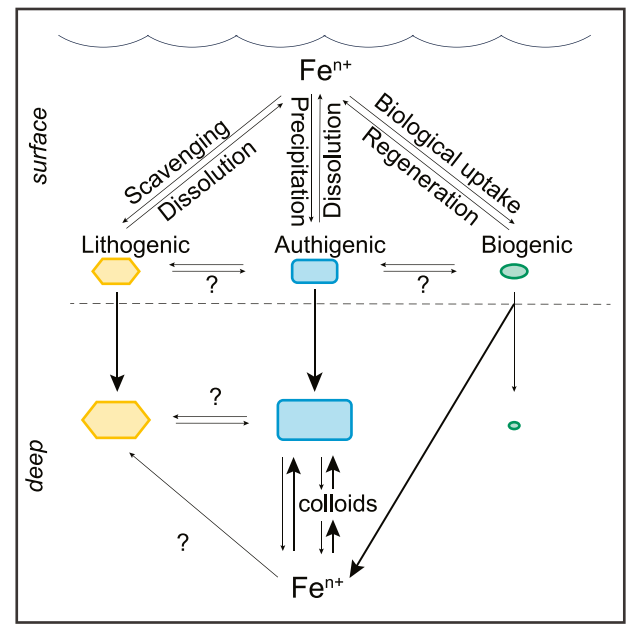
SOFEN ET AL. 16 of 23

9449224, 2023, 12, Downloaded from https://agupubs.onlinelibrary.wiley.com/doi/10.1029/2023GB007837, Wiley Online Library on [14/12/2023]. See the Terms

(a) Particle filters and single-cell measurements



(b) Particle cycling processes



(c) Iron concentration profiles

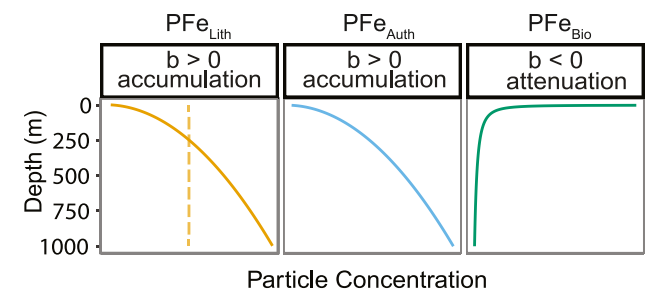


Figure 9. Particulate Fe fractions. (a) Experimental approach to measuring PFe fractions. (b) Conceptual diagram of proposed particulate iron phases and cycling processes, with the relative size of each phase indicating the relative concentration. Colloids are not shown on the surface due to space limitations. (c) Iron concentration profiles observed at Bermuda Atlantic Time-series Study. The dashed line vertical lithogenic profile represents the expectation (not observed) that the chemically refractory fraction would show no accumulation or attenuation (b = 0).

particles and scavenging of DFe as oxide coatings on pre-existing particles in the water column (Figure 9b). Mechanistic modeling work has demonstrated the importance of the first mechanism in the BATS region (Tagliabue et al., 2023) with the aggregation of colloidal Fe (oxyhydr)-oxides decoupled from organic ligands, a major source of PFe_{Auth}. To evaluate this mechanism in the field data, we compared profiles of PFe_{Auth} and CFe also measured at BATS during the BAIT cruises (Figure 5b). The similarity of these profiles is consistent with this "colloidal shunt" acting as an important link between DFe and PFe. However, comparison of moving-average *b* values for CFe (Figure 4) and PFe_{Auth} shows greater accumulation of the latter with depth, suggesting that surface scavenging also contributes to PFe_{Auth} formation.

The authigenic PFe fraction needs further direct study to understand whether its availability, solubility, and transport differ from other particulate phases. The chemical leach suggests higher solubility and bioavailability than the lithogenic fraction, although Kunde et al. (2019) propose that colloids are preferentially scavenged rather than taken up biologically in order to explain similar trends observed with colloidal Fe minima around the DCM. Data from the RESPIRE particle interceptor/incubator experiments also showed an increasing role for scavenging with depth (Bressac et al., 2019), but this study only considered biogenic and lithogenic phases. As oxyhydroxides age, they may become more refractory (Schlosser et al., 2018), and thus scavenged Fe may eventually move from the labile abiotic (authigenic) PFe pool to a more refractory PFe pool where it may be assessed operationally as lithogenic. Thus, the increasing refractory concentrations with depth may be due not only to slower sinking and lateral inputs (see discussion above) but also aging of scavenged Fe associated with slower sinking particles. The fate of authigenic Fe and the connections between age and lability therefore have implications for DFe inventories.

4.3. Authigenic Particulate Iron Is Important Across Productivity Gradients

Based on our finding of significant PFe Auth at BATS, as well as model simulations of the importance of the authigenic Fe phase there and in other regions (Tagliabue et al., 2023), we examined this fraction in other oceanic environments. The BATS site in the Sargasso Sea is extremely oligotrophic and very dusty, and it is therefore perhaps unsurprising that little Fe is associated with biogenic particles. Data that has been collected in different oceanic environments were examined to understand whether the contribution of PFe Auth varies with biological productivity and lithogenic inputs. Thus, we compiled data from three other cruises in four different environments: the SOTS study site in Fe-limited sub-Antarctic waters (SOTS), coastal California upwelling (IrnBru), and Arctic near-shore and off-shore sites (Arctic GEOTRACES). We compared discrete measurements from the upper 200 m instead of integrated inventories due to limited depth resolution from some of these studies. Our analysis suggests little difference in the partitioning of PFe pools across these different ocean regions; surprisingly, the estimate of PFe_{Auth} contribution at BATS may in fact represent a lower bound for the global ocean despite high dust input and low biological productivity in the Sargasso Sea.

Across all examined regions, PFe_{Bio} did not account for all of the chemically labile PFe pool, and PFe_{Bio} concentrations were consistent with previous estimates a superscript of the chemically labeled and the chemically labeled as the constant of the chemically labeled as the chemical property of the chemically labeled as the chemical property of the chemica

mates that the surface ocean biotic PFe pool is ca. 100 pM globally (Boyd et al., 2015). PFe_{Auth} at SOTS and IrnBru sites was a major component of the PFe pool in the upper 200 m and increased steadily with depth. In

SOFEN ET AL. 17 of 23

contrast, Marsay et al. (2017) found PFe $_{Auth}$ to be negligible at the surface of the Ross Sea but comprise up to 70% of PFe $_{Total}$ lower in the water column, with especially high concentrations with a range of sediment resuspension from the bottom. Despite a 300-fold difference in PFe $_{Total}$ concentrations between these different study regions, the proportion of PFe $_{Total}$ that was authigenic was comparable, ca. 20%–27%. This is slightly below the upper limit of PFe $_{Auth}$ (38 \pm 4% of PFe $_{Total}$, 100–200 m) reported by Black et al. (2020) in their global analysis. The PFe pools in the South Pacific and Arctic regions consisted of proportionally more PFe $_{Auth}$ (ca. 36%–55%), especially near shore, as shown by Xiang and Lam (2020) in the Arctic. High productivity over the shelf creates a high demand for electron acceptors to oxidize organic matter, resulting in the reduction of Fe and subsequent formation of (oxyhydr)oxides. Thus, additional Fe $_{Auth}$ may arise from direct precipitation. The use of region-specific cellular quotas, which were higher in Fe-replete regions, strengthens this conclusion. Similar calculations using a global mean Fe:C would have found artificially small biogenic fractions and more PFe $_{Auth}$ in the high-Fe regions. Our measurements represent a higher likely biogenic fraction yet still find PFe $_{Auth}$ to dominate. The trend toward proportionally higher PFe $_{Auth}$ in Fe-rich regions is consistent with the model of Boyd et al. (2010) showing more scavenging at higher Fe. The relative contributions of these processes will require further direct measurement in order to understand the dynamics that maintain the relatively consistent PFe $_{Auth}$ fraction.

4.4. Refractory Fe Provides a Robust Estimate of Lithogenic Fe

The errors and analytical challenges inherent to operational phase definitions led us to assess multiple approaches for determining the PFe Aurh pool. Our operational estimates may err in two ways: (a) by including refractory material that is not lithogenic, and (b) by omitting lithogenic material that is not refractory. We compared PFe_{1 ib} from the total-leach and proxy methods. We used PAI rather than PTi for a lithogenic proxy because approximately half our particle samples had PTi concentrations below the limit of detection. Aluminum recoveries for metalrich certified reference materials BCR-14 and PACS-2 were below 100% (82 \pm 4% and 59 \pm 10%, respectively, Table S3 in Supporting Information S1), despite good Fe recoveries (104% and 95%). If PAI and PFe measurements were corrected for recoveries, the resulting Fe:Al ratios would be lower, 62%-79% of the reported values (PACS-2 and BCR-14 corrections, respectively). We nevertheless have confidence in the PAI measurements of the field samples because Fe:Al ratios agree with concurrently collected, and independently analyzed, aerosol samples (Figure 6). Nonetheless, Al is an imperfect lithogenic tracer because it is both abiotically scavenged (Ohnemus & Lam, 2015) and potentially subject to biological uptake by diatoms (Moran & Moore, 1992). The low diatom abundance in the BATS region suggests this process will be minor, and an estimate of Al_{anal} from the BATS BSi climatology shows that diatoms likely constituted only 1%-3% of PAI_{Total} (not accounting for surface adsorption). Furthermore, diatom influence would also cause elevated PAI:PTi, but consistently high PAI:PTi was not observed in the euphotic zone. Importantly, PFe_{Lith} increases with depth using either PFe_{Refrac} or PAl_{Total} to estimate this fraction, and comparable moving-average b values for PAl_{Total} and PFe_{Refrac} suggest similar rates of particle accumulation at depth, supporting the use of either the total-leach or proxy method to measure PFe_{Lith}

The proxy method requires an appropriate choice of Fe:Al_{Source} for the lithogenic source inputs. In the BATS region, PFe_{Lith} in the upper 200 m reflected seasonal processes, whereas below 200 m this PFe fraction was relatively consistent across seasons. Aerosol deposition was highest from June to September (Sedwick et al., 2023), producing elevated surface PFe_{Lith} in August. Aerosol source regions also shifted with season: previous (2009–2010) air mass back trajectories in the region indicate a North American influence in the winter and African/European influence in the summer (Fishwick et al., 2014; Sedwick et al., 2007). Measured PFe_{Refrac}:PAI_{Total} in water column and aerosol particles was lower than for North African dust, North American, and European aerosol reference values (Shelley et al., 2015). The poor regression fit for March, May, and November data suggests multiple populations of lithogenic particles corresponding to different end members and/or different labilities or solubilities (Shelley et al., 2018). Our results are consistent with the impact of high African dust inputs during the summer and lower, more variably-sourced inputs during other seasons. This hypothesis could be assessed with size-fractionated particle data to determine whether inputs are dominated by larger, fast-sinking dust in the summer and smaller, longer-residence pollution aerosols in winter.

Lithogenic source region variability introduces uncertainty to estimates of lithogenic elemental proxies and highlights the utility of chemical leaches. Using Fe:Al_{UCC} alone would predict PFe_{Lith} similar to PFe_{Refrac} during dusty months but in excess of measured PFe_{Total} in 16% of bottle measurements (mostly for March and May samples). The problem is exacerbated if only North Atlantic aerosol values for Fe:Al are used: PFe_{Lith} would be determined

SOFEN ET AL. 18 of 23

to be in excess of PFe_{Total} in 30% of our bottle samples. The median excess is 55% greater than PFe_{Total} and would be greater if corrected for the low Al recoveries discussed above. A similar issue was recently reported by Black et al. (2020), leading them to assume a 20% uncertainty in PFe_{Lith} calculations owing to the variability in Fe:Al. Their estimates of PFe_{Lith} in the BATS region using Al as a lithogenic tracer found large particles enriched in Fe (Fe:Al 0.21–0.3 mol/mol), which corresponded to high lithogenic Fe (Black et al., 2020). In our study, water column PFe_{Refrac}:PAl_{Total} was within 22% of the UCC Fe:Al_{Source} average (Rudnick & Gao, 2003), 25%–92% less than North African aerosol values measured during GA03 (Shelley et al., 2018), and within 25% of ratios measured in concurrently collected aerosols (except in May, where aerosol was more than two-fold enriched in Fe). This was sufficiently different from the reference values to question the validity of using a single end member ratio. While previous studies have successfully used two end members to fit field data (e.g., Tagliabue et al., 2019), we chose to apply the total-leach method to avoid the uncertainties outlined above.

Within the water column, the observed increase in PFe_{Lith} with depth may be due to a decrease in particle size and associated slower sinking rates at depth or lateral subsurface inputs. We observed a minimum in PFe_{Lith} at the DCM, indicating the dominance of removal processes over sources (Ohnemus & Lam, 2015). Below the euphotic zone, lithogenic material partitions into smaller particles (Ohnemus & Lam, 2015) that likely sink more slowly, thus leading to higher concentrations. Alternatively, higher concentrations at depth might reflect lateral inputs from the North American shelf, as occasionally seen between 500 and 1,500 m in particle trap fluxes (Conte et al., 2019). Such inputs should also be evident in Fe:Al ratios if significantly different from aerosol inputs, but we saw no consistent trends in Fe:Al profiles in this depth range. Lateral inputs would cause higher local moving-average b values corresponding to particle accumulation, but this was also not observed. In fact, moving-average b values tended to be slightly lower from 500 to 1,000 m than they were at the surface in May through November. Finally, lateral inputs should also be observable by beam attenuation (Hwang, Manganini, et al., 2009; Hwang, Montluçon, & Eglinton, 2009) but no clear signal was seen in any month (Figure S3 in Supporting Information S1). Together, this is more consistent with accumulation due to slower sinking rates rather than lateral inputs, but both may contribute.

The concentrations of PFe $_{Total}$ and PFe $_{Lith}$ were highly heterogeneous between depths in the upper water column in March, consistent with the short residence times reported previously for these species. During the PEACETIME study in the Mediterranean Sea, PFe $_{Total}$ inventories in the upper 200 m decreased by more than 40% from 1.2 to 0.7 nmol/m 2 over 2–3 days after wet deposition events (Bressac et al., 2021). High variability in March fluxes at 500 m depth have been observed in particle traps in March, with fluxes as much as six times higher than usual in some years (Conte et al., 2019). Given the high variability of this region, the concurrent measurement of PFe $_{Refrac}$ with other Fe cycle parameters was key to constraining this fraction's proportional contribution.

5. Conclusions and Perspectives on Future Research

Constraining particulate pools with direct measurements of refractory, labile, and biogenic pools confirms that the authigenic fraction of PFe is a major component of the ocean Fe cycle (Figure 9). These results are supported by process study observations and recent biogeochemical modeling that demonstrates that colloidal aggregation into PFe_{Auth} is a critical component of ocean Fe dynamics (Tagliabue et al., 2023). Furthermore, our measurements confirm that these fractions have unique behaviors, with PFe_{Bio} remineralized below the PPZ and PFe_{Lith} and PFe_{Auth} fractions increasing with depth. It is likely that remineralized PFe_{Bio} contributes to PFe_{Auth} through colloid formation and aggregation and/or through adsorption onto other particles. This internal cycling decouples the net regeneration of PFe from other biomass elements such as P that are not subject to the same scavenging and solubility controls (Tagliabue et al., 2019). The different mechanisms of internal cycling are subject to different physical and chemical controls both in formation and reactivity.

In order to better understand the formation and reactivity of PFe_{Auth}, future work would benefit from a focus on understanding the variability in operational values of lithogenic and biogenic values used in its determination, and also measuring authigenic phases directly. Nanoscale spectroscopy, for instance, could be used to complement bulk particle characterization. Particles are highly heterogeneous, including crystalline and amorphous material as well as organic matter, and bulk methods cannot distinguish between authigenic and biogenic PFe phases. Authigenic PFe phases are thought to be composed of (oxyhydr)oxide minerals that are chemically labile to the acetic acid/hydroxylamine leach (Berger et al., 2008), yet bioavailability likely varies across minerals depending on the mineral structure. Synchrotron X-ray absorption spectroscopy (Jones et al., 2022; Shoenfelt et al., 2018; Toner et al., 2016) is well suited to identifying marine PFe mineral phases, and multiple methods in combination with targeted field

SOFEN ET AL. 19 of 23

19449224, 2023, 12, Downloaded from https://agupubs.onlinelibrary.wiley.com/doi/10.1029/2023GB007837, Wiley Online Library on [14/12/2023]. See the Terms and Conditions (https://onlinelibrary.wiley.com/terms/

and laboratory studies may answer lingering questions regarding the mineralogy of particles and the role of organic molecules in marine particle formation and stabilization (Hoffman et al., 2018; Lam et al., 2006). Microanalytical approaches may also help to address the size distribution and particle associations of authigenic Fe. Is this phase comprised mostly of Fe oxide coatings on other particles or of discrete Fe oxide minerals, either occurring individually or included in heterogeneous particle assemblages? Constraining the physical form of these chemical fractions will help to further improve the understanding and models of Fe behavior and bioavailability in the ocean.

Data Availability Statement

Phytoplankton stoichiometries from the Bermuda Atlantic Iron Time-series (BAIT) study are available from Zenodo at https://doi.org/10.5281/ZENODO.8305791 (Twining & Sofen, 2023). Particle elemental concentrations from the BAIT study are available from BCO-DMO at https://doi.org/10.26008/1912/bco-dmo.888772.1 (Twining et al., 2023). Supporting data provided by the BATS program are available at http://bats.bios.edu/ bats-data/. Dissolved trace element data from the BAIT study are available from BCO-DMO at https://doi. org/10.26008/1912/BCO-DMO.869081.1 (Buck & Caprara, 2023). Aerosol and dissolved trace element data from the BAIT study were previously published by Sedwick et al. (2023). Elemental contents of phytoplankton and particles at the Southern Ocean Time Series site are available from the Zenodo data repository at https://doi.org/10.5281/zenodo.5191479 (Sofen & Twining, 2021) and https://doi.org/10.5281/zenodo.7703343 (Twining, 2023a), respectively. Elemental contents of phytoplankton and particles from the IrnBru project are available from BCO-DMO at https://doi.org/10.26008/1912/bco-dmo.841583.1 (Twining, 2021) and https://doi. org/10.26008/1912/bco-dmo.6631983.1 (Twining, 2016), respectively. Particulate elemental concentrations from the Arctic GT cruise GN01 are available from GEOTRACES IDP2021 at https://www.geotraces.org/geotraces-intermediate-data-product-2021/ (GEOTRACES Intermediate Data Product Group, 2023). Arctic phytoplankton stoichiometries are available from BCO-DMO at https://doi.org/10.26008/1912/bco-dmo.904895.1 (Twining, 2023b).

References

Al-Hashem, A. A., Beck, A. J., Krisch, S., Menzel Barraqueta, J., Steffens, T., & Achterberg, E. P. (2022). Particulate trace metal sources, cycling, and distributions on the southwest African shelf. *Global Biogeochemical Cycles*, 36(11), e2022GB007453. https://doi.org/10.1029/2022GB007453

Berger, C. J. M., Lippiatt, S. M., Lawrence, M. G., & Bruland, K. W. (2008). Application of a chemical leach technique for estimating labile particulate aluminum, iron, and manganese in the Columbia River plume and coastal waters off Oregon and Washington. *Journal of Geophysical Research*, 113(C2), C00B01. https://doi.org/10.1029/2007JC004703

Black, E. E., Kienast, S. S., Lemaitre, N., Lam, P. J., Anderson, R. F., Planquette, H., et al. (2020). Ironing out Fe residence time in the dynamic upper ocean. *Global Biogeochemical Cycles*, 34(9), e2020GB006592. https://doi.org/10.1029/2020GB006592

Boyd, P. W., & Ellwood, M. J. (2010). The biogeochemical cycle of iron in the ocean. *Nature Geoscience*, 3(10), 675–682. https://doi.org/10.1038/ngeo964

Boyd, P. W., Ellwood, M. J., Tagliabue, A., & Twining, B. S. (2017). Biotic and abiotic retention, recycling and remineralization of metals in the ocean. *Nature Geoscience*, 10(3), 167–173. https://doi.org/10.1038/ngeo2876

Boyd, P. W., Ibisanmi, E., Sander, S. G., Hunter, K. A., & Jackson, G. A. (2010). Remineralization of upper ocean particles: Implications for iron biogeochemistry. *Limnology & Oceanography*, 55(3), 1271–1288. https://doi.org/10.4319/lo.2010.55.3.1271

Boyd, P. W., Strzepek, R. F., Ellwood, M. J., Hutchins, D. A., Nodder, S. D., Twining, B. S., & Wilhelm, S. W. (2015). Why are biotic iron pools uniform across high- and low-iron pelagic ecosystems? Pelagic Biota and iron biogeochemistry. *Global Biogeochemical Cycles*, 29(7), 1028–1043. https://doi.org/10.1002/2014GB005014

Bressac, M., Guieu, C., Ellwood, M. J., Tagliabue, A., Wagener, T., Laurenceau-Cornec, E. C., et al. (2019). Resupply of mesopelagic dissolved iron controlled by particulate iron composition. *Nature Geoscience*, 12, 995–1000. https://doi.org/10.1038/s41561-019-0476-6

Bressac, M., Wagener, T., Leblond, N., Tovar-Sánchez, A., Ridame, C., Taillandier, V., et al. (2021). Subsurface iron accumulation and rapid aluminum removal in the Mediterranean following African dust deposition. *Biogeosciences*, 18(24), 6435–6453. https://doi.org/10.5194/bg-18-6435-2021

Bruland, K. W., Donat, J. R., & Hutchins, D. A. (1991). Interactive influences of bioactive trace metals on biological production in oceanic waters. Limnology & Oceanography, 36(8), 1555–1577. https://doi.org/10.4319/lo.1991.36.8.1555

Buat-Menard, P., & Chesselet, R. (1979). Variable influence of the atmospheric flux on the trace metal chemistry of oceanic suspended matter. Earth and Planetary Science Letters, 42(3), 399–411. https://doi.org/10.1016/0012-821X(79)90049-9

Buck, K., & Caprara, S. (2023). Dissolved iron speciation results from 2019 Bermuda Atlantic iron Time-series (BAIT) cruises EN631, AE1909, AE1921, AE1930 in the Western subtropical North Atlantic Gyre from March to November 2019 (BAIT Project) [Dataset]. BCO-DMO. https://doi.org/10.26008/1912/BCO-DMO.869081.1

Cohen, N. R., Ellis, K. A., Lampe, R. H., McNair, H., Twining, B. S., Maldonado, M. T., et al. (2017). Diatom transcriptional and physiological responses to changes in iron bioavailability across ocean provinces. Frontiers in Marine Science, 4, 360. https://doi.org/10.3389/fmars.2017.00360

Conte, M. H., Carter, A. M., Koweek, D. A., Huang, S., & Weber, J. C. (2019). The elemental composition of the deep particle flux in the Sargasso Sea. Chemical Geology, 511, 279–313. https://doi.org/10.1016/j.chemgeo.2018.11.001

Acknowledgments

The BAIT work was supported by US National Science Foundation awards OCE-1829818 to BST and DCO, OCE-2023237 to BST, OCE-1829833 to PNS, OCE-1829777 to KNB, and OCE-1829844 to R.I. and UK National Environment Research Council award NE/S013547/1 to AT. Use of the Advanced Photon Source, an Office of Science User Facility operated for the U.S. Department of Energy (DOE) Office of Science by Argonne National Laboratory, was supported by the U.S. DOE under Contract No. DE-AC02-06CH11357. We gratefully acknowledge the assistance of the crew and marine technicians aboard RV Endeavor and RV Atlantic Explorer, BATS research team for sampling efforts, as well as Dominic Smith for calculations of the mixed layer depth and BATS PIs (Bates, Johnson, Lomas, and Steinberg), We thank Bettina Sohst for sample collection during the BAIT cruises and for analysis of aerosol samples, and Tara Williams for processing the aerosol samples. We thank Adrian Marchetti, Natalie Cohen, and Claire Till for measurements during the IrnBru cruise. The Arctic particle data is included in the GEOTRACES 2021 Intermediate Data Product (IDP2021). which represents an international collaboration and is endorsed by the Scientific Committee on Oceanic Research (SCOR). The many researchers and funding agencies responsible for the collection of data and quality control are thanked for their contributions to the IDP2021. The paper was significantly improved by constructive comments provided by Phoebe Lam and two anonymous reviewers.

SOFEN ET AL. 20 of 23



Global Biogeochemical Cycles

- 10.1029/2023GB007837
- Cutter, G., Casciotti, K., Croot, P., Geibert, W., Heimburger, L.-E., Lohan, M., et al. (2017). Sampling and sample-handling protocols for GEOTRACES cruises. GEOTRACES International Project Office. https://dx.doi.org/10.25607/OBP-2
- Eriksen, R., Trull, T., Davies, D., Jansen, P., Davidson, A., Westwood, K., & van den Enden, R. (2018). Seasonal succession of phytoplankton community structure from autonomous sampling at the Australian Southern Ocean Time Series (SOTS) observatory. *Marine Ecology Progress Series*, 589, 13–31. https://doi.org/10.3354/meps12420
- Fishwick, M. P., Sedwick, P. N., Lohan, M. C., Worsfold, P. J., Buck, K. N., Church, T. M., & Ussher, S. J. (2014). The impact of changing surface ocean conditions on the dissolution of aerosol iron. *Global Biogeochemical Cycles*, 28(11), 1235–1250. https://doi.org/10.1002/2014GB004921
- GEOTRACES Intermediate Data Product Group. (2023). The GEOTRACES intermediate data Product 2021 version 2 (IDP2021v2). NERC EDS British Oceanographic Data Centre NOC. https://doi.org/10.5285/cf2d9ba9-d51d-3b7c-e053-8486abc0f5fd
- Gilbert, N. E., LeCleir, G. R., Strzepek, R. F., Ellwood, M. J., Twining, B. S., Roux, S., et al. (2022). Bioavailable iron titrations reveal oceanic Syne-chococcus ecotypes optimized for different iron availabilities. ISME Communications, 2(1), 54. https://doi.org/10.1038/s43705-022-00132-5
- Goldberg, E. D. (1954). Marine geochemistry 1. Chemical scavengers of the sea. The Journal of Geology, 62(3), 249–265. https://doi.org/10.1086/626161
- Gourain, A., Planquette, H., Cheize, M., Lemaitre, N., Menzel Barraqueta, J.-L., Shelley, R., et al. (2019). Inputs and processes affecting the distribution of particulate iron in the North Atlantic along the GEOVIDE (GEOTRACES GA01) section. *Biogeosciences*, 16(7), 1563–1582. https://doi.org/10.5194/bg-16-1563-2019
- Hahn-Woernle, L., Dijkstra, H. A., & Van der Woerd, H. J. (2014). Sensitivity of phytoplankton distributions to vertical mixing along a North Atlantic transect. Ocean Science, 10(6), 993–1011. https://doi.org/10.5194/os-10-993-2014
- Hoffman, C. L., Nicholas, S. L., Ohnemus, D. C., Fitzsimmons, J. N., Sherrell, R. M., German, C. R., et al. (2018). Near-field iron and carbon chemistry of non-buoyant hydrothermal plume particles, Southern East Pacific Rise 15°S. Marine Chemistry, 201, 183–197. https://doi.org/10.1016/j.marchem.2018.01.011
- Hollister, A. P., Kerr, M., Malki, K., Muhlbach, E., Robert, M., Tilney, C. L., et al. (2020). Regeneration of macronutrients and trace metals during phytoplankton decay: An experimental study. *Limnology & Oceanography*, 65(8), 1936–1960. https://doi.org/10.1002/lno.11429
- Hopkinson, B. M., & Barbeau, K. A. (2008). Interactive influences of iron and light limitation on phytoplankton at subsurface chlorophyll maxima in the eastern North Pacific. *Limnology & Oceanography*, 53(4), 1303–1318. https://doi.org/10.4319/lo.2008.53.4.1303
- Hurst, M. P., Aguilar-Islas, A. M., & Bruland, K. W. (2010). Iron in the southeastern Bering Sea: Elevated leachable particulate Fe in shelf bottom waters as an important source for surface waters. Continental Shelf Research, 30(5), 467–480. https://doi.org/10.1016/j.csr.2010.01.001
- Hurst, M. P., & Bruland, K. W. (2007). An investigation into the exchange of iron and zinc between soluble, colloidal, and particulate size-fractions in shelf waters using low-abundance isotopes as tracers in shipboard incubation experiments. *Marine Chemistry*, 103(3–4), 211–226. https://doi.org/10.1016/j.marchem.2006.07.001
- Hwang, J., Manganini, S. J., Montluçon, D. B., & Eglinton, T. I. (2009). Dynamics of particle export on the Northwest Atlantic margin. *Deep Sea Research Part I: Oceanographic Research Papers*, 56(10), 1792–1803. https://doi.org/10.1016/j.dsr.2009.05.007
- Hwang, J., Montluçon, D., & Eglinton, T. I. (2009). Molecular and isotopic constraints on the sources of suspended particulate organic carbon on the northwestern Atlantic margin. Deep Sea Research Part I: Oceanographic Research Papers, 56(8), 1284–1297. https://doi.org/10.1016/j. dsr 2009 01 012
- Jensen, L. T., Morton, P., Twining, B. S., Heller, M. I., Hatta, M., Measures, C. I., et al. (2020). A comparison of marine Fe and Mn cycling: U.S. GEOTRACES GN01 Western Arctic case study. Geochimica et Cosmochimica Acta, 288, 138–160. https://doi.org/10.1016/j.gca.2020.08.006
- Jones, R., Nicholas, S., Northrup, P., Bostick, B., Hoffman, C., Hu, W., et al. (2022). Characterization and speciation of marine materials using synchrotron probes: Guidelines for new users. *Oceanography*, 35(2), 49–54. https://doi.org/10.5670/oceanog.2022.207
- King, A. L., Buck, K. N., & Barbeau, K. A. (2012). Quasi-Lagrangian drifter studies of iron speciation and cycling off point conception, California. Marine Chemistry, 128–129, 1–12. https://doi.org/10.1016/j.marchem.2011.11.001
- Kunde, K., Wyatt, N. J., González-Santana, D., Tagliabue, A., Mahaffey, C., & Lohan, M. C. (2019). Iron distribution in the subtropical North Atlantic: The pivotal role of colloidal iron. *Global Biogeochemical Cycles*, 33(12), 1532–1547. https://doi.org/10.1029/2019GB006326
- Lam, P. J., Bishop, J. K. B., Henning, C. C., Marcus, M. A., Waychunas, G. A., & Fung, I. Y. (2006). Wintertime phytoplankton bloom in the subarctic Pacific supported by continental margin iron: Continental margin Fe delivery to subarctic pacific. *Global Biogeochemical Cycles*, 20(1), GB1006. https://doi.org/10.1029/2005GB002557
- Lam, P. J., Doney, S. C., & Bishop, J. K. B. (2011). The dynamic ocean biological pump: Insights from a global compilation of particulate organic carbon, CaCO₃, and opal concentration profiles from the mesopelagic: The dynamic ocean biological pump. *Global Biogeochemical Cycles*, 25, GB3009. https://doi.org/10.1029/2010GB003868
- Lam, P. J., Lee, J.-M., Heller, M. I., Mehic, S., Xiang, Y., & Bates, N. R. (2018). Size-fractionated distributions of suspended particle concentration and major phase composition from the U.S. GEOTRACES Eastern Pacific Zonal Transect (GP16). Marine Chemistry, 201, 90–107. https://doi.org/10.1016/j.marchem.2017.08.013
- Lampe, R. H., Mann, E. L., Cohen, N. R., Till, C. P., Thamatrakoln, K., Brzezinski, M. A., et al. (2018). Different iron storage strategies among bloom-forming diatoms. Proceedings of the National Academy of Sciences of the United States of America, 115(52), E12275–E12284. https://doi.org/10.1073/pnas.1805243115
- Landing, W. M., & Bruland, K. W. (1987). The contrasting biogeochemistry of iron and manganese in the Pacific Ocean. Geochimica et Cosmochimica Acta, 51(1), 29–43. https://doi.org/10.1016/0016-7037(87)90004-4
- Lemaitre, N., Planquette, H., Dehairs, F., Planchon, F., Sarthou, G., Gallinari, M., et al. (2020). Particulate trace element export in the North Atlantic (GEOTRACES GA01 transect, GEOVIDE cruise). ACS Earth and Space Chemistry, 4(11), 2185–2204. https://doi.org/10.1021/acsearthspacechem.0c00045
- Lemaitre, N., Planquette, H., Dehairs, F., Van Der Merwe, P., Bowie, A. R., Trull, T. W., et al. (2016). Impact of the natural Fe-fertilization on the magnitude, stoichiometry and efficiency of particulate biogenic silica, nitrogen and iron export fluxes. *Deep Sea Research Part I: Ocean-ographic Research Papers*, 117, 11–27. https://doi.org/10.1016/j.dsr.2016.09.002
- Lomas, M. W., Baer, S. E., Mouginot, C., Terpis, K. X., Lomas, D. A., Altabet, M. A., & Martiny, A. C. (2021). Varying influence of phytoplank-ton biodiversity and stoichiometric plasticity on bulk particulate stoichiometry across ocean basins. *Communications Earth & Environment*, 2(1), 143. https://doi.org/10.1038/s43247-021-00212-9
- Lomas, M. W., Bates, N. R., Johnson, R. J., Steinberg, D. K., & Tanioka, T. (2022). Adaptive carbon export response to warming in the Sargasso Sea. *Nature Communications*, 13(1), 1211. https://doi.org/10.1038/s41467-022-28842-3
- Marsay, C. M., & Achterberg, E. P. (2021). Particulate iron and other trace elements in near-surface waters of the high latitude North Atlantic following the 2010 Eyjafjallajökull eruption. *Marine Chemistry*, 232, 103959. https://doi.org/10.1016/j.marchem.2021.103959
- Marsay, C. M., Aguilar-Islas, A., Fitzsimmons, J. N., Hatta, M., Jensen, L. T., John, S. G., et al. (2018). Dissolved and particulate trace elements in late summer Arctic melt ponds. *Marine Chemistry*, 204, 70–85. https://doi.org/10.1016/j.marchem.2018.06.002

SOFEN ET AL. 21 of 23

- Marsay, C. M., Barrett, P. M., McGillicuddy, D. J., & Sedwick, P. N. (2017). Distributions, sources, and transformations of dissolved and particulate iron on the Ross Sea continental shelf during summer. *Journal of Geophysical Research: Oceans*, 122(8), 6371–6393. https://doi.org/10.1002/2017JC013068
- Martin, J. H., & Knauer, G. A. (1973). The elemental composition of plankton. Geochimica et Cosmochimica Acta, 37(7), 1639–1653. https://doi.org/10.1016/0016-7037(73)90154-3
- Martin, J. H., Knauer, G. A., Karl, D. M., & Broenkow, W. W. (1987). VERTEX: Carbon cycling in the northeast Pacific. *Deep Sea Research Part A. Oceanographic Research Papers*, 34(2), 267–285. https://doi.org/10.1016/0198-0149(87)90086-0
- Martin, P., Dyhrman, S. T., Lomas, M. W., Poulton, N. J., & Van Mooy, B. A. S. (2014). Accumulation and enhanced cycling of polyphosphate by Sargasso Sea plankton in response to low phosphorus. *Proceedings of the National Academy of Sciences of the United States of America*, 111(22), 8089–8094. https://doi.org/10.1073/pnas.1321719111
- Martiny, A. C., Pham, C. T. A., Primeau, F. W., Vrugt, J. A., Moore, J. K., Levin, S. A., & Lomas, M. W. (2013). Strong latitudinal patterns in the elemental ratios of marine plankton and organic matter. *Nature Geoscience*, 6(4), 279–283. https://doi.org/10.1038/ngeo1757
- Menden-Deuer, S., & Lessard, E. J. (2000). Carbon to volume relationships for dinoflagellates, diatoms, and other protist plankton. Limnology & Oceanography, 45(3), 569–579. https://doi.org/10.4319/lo.2000.45.3.0569
- Milne, A., Schlosser, C., Wake, B. D., Achterberg, E. P., Chance, R., Baker, A. R., et al. (2017). Particulate phases are key in controlling dissolved iron concentrations in the (sub)tropical North Atlantic. *Geophysical Research Letters*, 44(5), 2377–2387. https://doi.org/10.1002/2016GL072314
- Moran, S. B., & Moore, R. M. (1992). Kinetics of the removal of dissolved aluminum by diatoms in seawater: A comparison with thorium. Geochimica et Cosmochimica Acta, 56(9), 3365–3374. https://doi.org/10.1016/0016-7037(92)90384-U
- Ohnemus, D. C., Auro, M. E., Sherrell, R. M., Lagerström, M., Morton, P. L., Twining, B. S., et al. (2014). Laboratory intercomparison of marine particulate digestions including Piranha: A novel chemical method for dissolution of polyethersulfone filters. *Limnology & Oceanography*, 12(8), 530–547. https://doi.org/10.4319/lom.2014.12.530
- Ohnemus, D. C., & Lam, P. J. (2015). Cycling of lithogenic marine particles in the US GEOTRACES North Atlantic transect. *Deep Sea Research Part II: Topical Studies in Oceanography*, 116, 283–302. https://doi.org/10.1016/j.dsr2.2014.11.019
- Ohnemus, D. C., Torrie, R., & Twining, B. S. (2019). Exposing the distributions and elemental associations of scavenged particulate phases in the ocean using basin-scale multi-element data sets. *Global Biogeochemical Cycles*, 33(6), 725–748. https://doi.org/10.1029/2018GB006145
- Owens, S. A., Pike, S., & Buesseler, K. O. (2015). Thorium-234 as a tracer of particle dynamics and upper ocean export in the Atlantic Ocean. Deep Sea Research Part II: Topical Studies in Oceanography, 116, 42–59. https://doi.org/10.1016/j.dsr2.2014.11.010
- Rafter, P. A., Sigman, D. M., & Mackey, K. R. M. (2017). Recycled iron fuels new production in the eastern equatorial Pacific Ocean. *Nature Communications*, 8(1), 1100. https://doi.org/10.1038/s41467-017-01219-7
- Rauschenberg, S., & Twining, B. S. (2015). Evaluation of approaches to estimate biogenic particulate trace metals in the ocean. *Marine Chemistry*, 171, 67–77. https://doi.org/10.1016/j.marchem.2015.01.004
- R Core Team. (2022). R: A language and environment for statistical computing. R Foundation for Statistical Computing.
- RStudio Team. (2021). RStudio: Integrated development environment for R. RStudio, PBC.
- Rudnick, R. L., & Gao, S. (2003). 3.01 composition of the continental crust. In Treatise on geochemistry (pp. 1–64). Elsevier.
- Saito, M. A., Noble, A., Hawco, N., Twining, B. S., Ohnemus, D. C., John, S. G., et al. (2016). The Acceleration of dissolved Cobalt's ecological stoichiometry due to biological uptake, remineralization, and scavenging in the Atlantic Ocean. *Biogeochemistry: Open Ocean*, 14(20), 4637–4662. https://doi.org/10.5194/bg-2016-511
- Schlosser, C., Schmidt, K., Aquilina, A., Homoky, W. B., Castrillejo, M., Mills, R. A., et al. (2018). Mechanisms of dissolved and labile particulate iron supply to shelf waters and phytoplankton blooms off South Georgia, Southern Ocean. *Biogeosciences*, 15(16), 4973–4993. https://doi.org/10.5194/bg-15-4973-2018
- Schmidt, K., Schlosser, C., Atkinson, A., Fielding, S., Venables, H. J., Waluda, C. M., & Achterberg, E. P. (2016). Zooplankton gut passage mobilizes lithogenic iron for ocean productivity. Current Biology, 26(19), 2667–2673. https://doi.org/10.1016/j.cub.2016.07.058
- Sedwick, P. N., Sholkovitz, E. R., & Church, T. M. (2007). Impact of anthropogenic combustion emissions on the fractional solubility of aerosol iron: Evidence from the Sargasso Sea: Fractional solubility of aerosol iron. *Geochemistry, Geophysics, Geosystems*, 8(10), Q10Q06. https://doi.org/10.1029/2007GC001586
- Sedwick, P. N., Sohst, B. M., Buck, K. N., Caprara, S., Johnson, R. J., Ohnemus, D. C., et al. (2023). Atmospheric input and seasonal inventory of dissolved iron in the Sargasso Sea: Implications for iron dynamics in surface Waters of the subtropical ocean. *Geophysical Research Letters*, 50(6), e2022GL102594. https://doi.org/10.1029/2022GL102594
- Shelley, R. U., Landing, W. M., Ussher, S. J., Planquette, H., & Sarthou, G. (2018). Regional trends in the fractional solubility of Fe and other metals from North Atlantic aerosols (GEOTRACES cruises GA01 and GA03) following a two-stage leach. *Biogeosciences*, 15(8), 2271–2288. https://doi.org/10.5194/bg-15-2271-2018
- Shelley, R. U., Morton, P. L., & Landing, W. M. (2015). Elemental ratios and enrichment factors in aerosols from the US-GEOTRACES North Atlantic transects. Deep Sea Research Part II: Topical Studies in Oceanography, 116, 262–272. https://doi.org/10.1016/j.dsr2.2014.12.005
- Sherrell, R. M., & Boyle, E. A. (1992). The trace metal composition of suspended particles in the oceanic water column near Bermuda. *Earth and Planetary Science Letters*, 111(1), 155–174. https://doi.org/10.1016/0012-821X(92)90176-V
- Shoenfelt, E. M., Winckler, G., Lamy, F., Anderson, R. F., & Bostick, B. C. (2018). Highly bioavailable dust-borne iron delivered to the Southern Ocean during glacial periods. *Proceedings of the National Academy of Sciences of the United States of America*, 115(44), 11180–11185. https://doi.org/10.1073/pnas.1809755115
- Sofen, L. E., Antipova, O. A., Ellwood, M. J., Gilbert, N. E., LeCleir, G. R., Lohan, M. C., et al. (2022). Trace metal contents of autotrophic flagellates from contrasting open-ocean ecosystems. *Limnol Oceanogr Letters*, 7(4), 354–362. https://doi.org/10.1002/lol2.10258
- Sofen, L. E., & Twining, B. S. (2021). Trace metal contents of autotrophic flagellates from contrasting open-ocean ecosystems [Dataset]. Zenodo. https://doi.org/10.5281/ZENODO.5191479
- Steinberg, D. K., & Landry, M. R. (2017). Zooplankton and the ocean carbon cycle. Annual Review of Marine Science, 9(1), 413–444. https://doi.org/10.1146/annurev-marine-010814-015924
- Sunda, W. G., & Huntsman, S. A. (1995). Iron uptake and growth limitation in oceanic and coastal phytoplankton. *Marine Chemistry*, 50(1–4), 189–206. https://doi.org/10.1016/0304-4203(95)00035-P
- Sunda, W. G., & Huntsman, S. A. (1997). Interrelated influence of iron, light and cell size on marine phytoplankton growth. *Nature*, 390(6658), 389–392. https://doi.org/10.1038/37093
- Tagliabue, A., Aumont, O., DeAth, R., Dunne, J. P., Dutkiewicz, S., Galbraith, E., et al. (2016). How well do global ocean biogeochemistry models simulate dissolved iron distributions? Global iron models. *Global Biogeochemical Cycles*, 30(2), 149–174. https://doi.org/10.1002/2015GR005289

SOFEN ET AL. 22 of 23

- Tagliabue, A., Bowie, A. R., DeVries, T., Ellwood, M. J., Landing, W. M., Milne, A., et al. (2019). The interplay between regeneration and scavenging fluxes drives ocean iron cycling. *Nature Communications*, 10(1), 4960. https://doi.org/10.1038/s41467-019-12775-5
- Tagliabue, A., Buck, K. N., Sofen, L. E., Twining, B. S., Aumont, O., Boyd, P. W., et al. (2023). Authigenic mineral phases as a driver of the upper-ocean iron cycle. *Nature*, 620(7972), 104–109. https://doi.org/10.1038/s41586-023-06210-5
- Taylor, S. R., & McLennan, S. M. (1995). The geochemical evolution of the continental crust. Review of Geophysics, 33(2), 241–265. https://doi.org/10.1029/95RG00262
- Toner, B. M., German, C. R., Dick, G. J., & Breier, J. A. (2016). Deciphering the complex chemistry of deep-ocean particles using complementary synchrotron X-ray microscope and microprobe instruments. *Accounts of Chemical Research*, 49(1), 128–137. https://doi.org/10.1021/acs.accounts.5b00282
- Tovar-Sanchez, A., Sañudo-Wilhelmy, S. A., Garcia-Vargas, M., Weaver, R. S., Popels, L. C., & Hutchins, D. A. (2003). A trace metal clean reagent to remove surface-bound iron from marine phytoplankton. *Marine Chemistry*, 82(1–2), 91–99. https://doi.org/10.1016/S0304-4203(03)00054-9
- Twining, B. S. (2016). Particulate data collected on R/V Melville (MV1405, IrnBru) along the California coast in July 2014 [Dataset]. BCO-DMO. https://doi.org/10.26008/1912/BCO-DMO.663183.1
- Twining, B. S. (2021). Element quotas of individual plankton cells collected during IRNBRU (MV1405) and June 2015 Line P cruises [Dataset]. BCO-DMO. https://doi.org/10.26008/1912/BCO-DMO.841583.1
- Twining, B. S. (2023a). SOTS particulate trace metal data [Dataset]. Zenodo. https://doi.org/10.5281/ZENODO.7703343
- Twining, B. S. (2023b). Element quotas of individual phytoplankton cells from samples collected on the US GEOTRACES Arctic cruise GN01 (HLY1502) on USCGC Healy in August-October 2015 [Dataset]. BCO-DMO. https://doi.org/10.26008/1912/BCO-DMO.904895.1
- Twining, B. S., Antipova, O., Chappell, P. D., Cohen, N. R., Jacquot, J. E., Mann, E. L., et al. (2021). Taxonomic and nutrient controls on phytoplankton iron quotas in the ocean. *Limnology & Oceanography*, 6(2), 96–106. https://doi.org/10.1002/jol2.10179
- Twining, B. S., & Baines, S. B. (2013). The trace metal composition of marine phytoplankton. *Annual Review of Marine Science*, 5(1), 191–215. https://doi.org/10.1146/annurev-marine-121211-172322
- Twining, B. S., Nodder, S. D., King, A. L., Hutchins, D. A., LeCleir, G. R., DeBruyn, J. M., et al. (2014). Differential remineralization of major and trace elements in sinking diatoms. *Limnology & Oceanography*, 59(3), 689–704. https://doi.org/10.4319/lo.2014.59.3.0689
- Twining, B. S., Nuñez-Milland, D., Vogt, S., Johnson, R. S., & Sedwick, P. N. (2010). Variations in *Synechococcus* cell quotas of phosphorus, sulfur, manganese, iron, nickel, and zinc within mesoscale eddies in the Sargasso Sea. *Limnology & Oceanography*, 55(2), 492–506. https://doi.org/10.4319/lo.2010.55.2.0492
- Twining, B. S., Ohnemus, D. C., & Sofen, L. (2023). Particulate trace element concentrations measured during four cruises in 2019 at locations around the Bermuda Atlantic Time-Series Study (BATS) station [Dataset]. BCO-DMO. https://doi.org/10.26008/1912/BCO-DMO.888772.1
- Twining, B. S., Rauschenberg, S., Baer, S. E., Lomas, M. W., Martiny, A. C., & Antipova, O. (2019). A nutrient limitation mosaic in the eastern tropical Indian Ocean. Deep Sea Research Part II: Topical Studies in Oceanography, 166, 125–140. https://doi.org/10.1016/j.dsr2.2019.05.001
- Twining, B. S., Rauschenberg, S., Morton, P. L., Ohnemus, D. C., & Lam, P. J. (2015). Comparison of particulate trace element concentrations in the North Atlantic Ocean as determined with discrete bottle sampling and in situ pumping. *Deep Sea Research Part II: Topical Studies in Oceanography*, 116, 273–282. https://doi.org/10.1016/j.dsr2.2014.11.005
- Twining, B. S., Rauschenberg, S., Morton, P. L., & Vogt, S. (2015). Metal contents of phytoplankton and labile particulate material in the North Atlantic Ocean. *Progress in Oceanography*, 137, 261–283. https://doi.org/10.1016/j.pocean.2015.07.001
- Twining, B. S., & Sofen, L. (2023). SXRF data for BAIT project [Dataset]. Zenodo. https://doi.org/10.5281/ZENODO.8305791
- van der Merwe, P., Wuttig, K., Holmes, T., Trull, T. W., Chase, Z., Townsend, A. T., et al. (2019). High lability Fe particles sourced from glacial erosion can meet previously unaccounted biological demand: Heard Island, Southern Ocean. Frontiers in Marine Science, 6, 332. https://doi.org/10.3389/fmars.2019.00332
- Wickham, H., Averick, M., Bryan, J., Chang, W., McGowan, L. D., François, R., et al. (2019). Welcome to the tidyverse. *Journal of Open Source Software*, 4(43), 1686. https://doi.org/10.21105/joss.01686
- Wilke, C. O. (2020). cowplot: Streamlined plot theme and plot annotations for "ggplot2" [Software]. R Foundation for Statistical Computing. Retrieved from https://CRAN.R-project.org/package=cowplot
- Xiang, Y., & Lam, P. J. (2020). Size-fractionated compositions of marine suspended Particles in the Western Arctic Ocean: Lateral and vertical sources. *Journal of Geophysical Research: Oceans*, 125(8), e2020JC016144. https://doi.org/10.1029/2020JC016144

References From the Supporting Information

- Casey, J. R., Aucan, J. P., Goldberg, S. R., & Lomas, M. W. (2013). Changes in partitioning of carbon amongst photosynthetic pico- and nano-plankton groups in the Sargasso Sea in response to changes in the North Atlantic Oscillation. *Deep Sea Research Part II: Topical Studies in Oceanography*, 93, 58–70. https://doi.org/10.1016/j.dsr2.2013.02.002
- de Boyer Montégut, C., Madec, G., Fischer, A. S., Lazar, A., & Iudicone, D. (2004). Mixed layer depth over the global ocean: An examination of profile data and a profile-based climatology. *Journal of Geophysical Research*, 109(C12), C12003. https://doi.org/10.1029/2004JC002378 ESRI ArcGIS Pro. (n.d.). How inverse weighted interpolation works. ESRI ArcGIS Pro.
- Frew, R. D., Hutchins, D. A., Nodder, S., Sanudo-Wilhelmy, S., Tovar-Sanchez, A., Leblanc, K., et al. (2006). Particulate iron dynamics during FeCycle in subantarctic waters southeast of New Zealand: FeCycle particle dynamics. Global Biogeochemical Cycles, 20(1), GB1S93. https://doi.org/10.1029/2005GB002558
- Hillebrand, H., Dürselen, C.-D., Kirschtel, D., Pollingher, U., & Zohary, T. (1999). Biovolume calculation for pelagic and benthic microalgae. Journal of Phycology, 35(2), 403–424. https://doi.org/10.1046/j.1529-8817.1999.3520403.x
- Moore, C. M., Mills, M. M., Arrigo, K. R., Berman-Frank, I., Bopp, L., Boyd, P. W., et al. (2013). Processes and patterns of oceanic nutrient limitation. *Nature Geoscience*, 6(9), 701–710. https://doi.org/10.1038/ngeo1765
- Vogt, S. (2003). MAPS: A set of software tools for analysis and visualization of 3D X-ray fluorescence data sets. *Journal de Physique IV* (*Proceedings*), 104, 635–638. https://doi.org/10.1051/jp4:20030160

SOFEN ET AL. 23 of 23